

1 **Strain Localization and Migration During the Pulsed Lateral Propagation**  
2 **of the Shire Rift Zone, East Africa**

3 Folarin Kolawole<sup>1,2\*</sup>, Travis Vick<sup>3,4</sup>, Estella A. Atekwana<sup>5</sup>, Daniel A. Laó-Dávila<sup>6</sup>, Aristides G.  
4 Costa<sup>3</sup>, and Brett M. Carpenter<sup>3</sup>

5 <sup>1</sup>BP Exploration, Houston, TX 77079

6 <sup>2</sup>Lamont-Doherty Earth Observatory at Columbia University, Palisades, NY 10964

7 <sup>3</sup>School of Geosciences, University of Oklahoma, Norman OK 73019

8 <sup>4</sup>Department of Geophysics, Colorado School of Mines, Golden, CO 80401

9 <sup>5</sup>Department of Earth and Planetary Sciences, University of California, Davis, CA 95616

10 <sup>6</sup>Boone Pickens School of Geology, Oklahoma State University, Stillwater, OK 74078

11

12 *\*Corresponding Author: folarin.kol@gmail.com*

13

14

15

16 **Key Points:**

17 **1)** Multiphase rifting in the Shire Rift Zone (SRZ) transitioned from earlier magma-rich  
18 phases (RP1 & 2) to the currently active magma-poor phase (RP3)

19

20 **2)** Surface and subsurface data suggest a pulsed lateral SRZ propagation with transient rift  
21 tip stagnation at/near rift-orthogonal basement shear zones

22

23 **3)** Inherited intra-basement structures served as both strain-localizing and temporary  
24 strain-inhibiting tectonic elements during the rift propagation

25

26

27

28

29

30

31

32

33

34

35

36 **Abstract**

37 We investigate the spatiotemporal patterns of strain accommodation during multiphase rift  
38 evolution in the Shire Rift Zone (SRZ), East Africa. The NW-trending SRZ records a transition  
39 from magma-rich rifting phases (Permian-Early Jurassic: Rift-Phase 1 (RP1), and Late  
40 Jurassic-Cretaceous: Rift-Phase 2 (RP2)) to a magma-poor phase in the Cenozoic (ongoing:  
41 Rift-Phase 3 (RP3)). Our observations show that although the rift border faults largely mimic  
42 the pre-rift basement metamorphic fabrics, the rift termination zones occur near crustal-  
43 scale rift-orthogonal basement shear zones (Sanangoe (SSZ) and the Lurio shear zones)  
44 during RP1-RP2. In RP3, the RP1-RP2 sub-basins were largely abandoned, and the rift axes  
45 migrated northeastward (rift-orthogonally) into the RP1-RP2 basin margin, and  
46 northwestward (strike-parallel) ahead of the RP2 rift-tip. The northwestern RP3 rift-axis  
47 side-steps across the SSZ, with a rotation of border faults across the shear zone and  
48 terminates further northwest at another regional-scale shear zone. We suggest that over the  
49 multiple pulses of tectonic extension and strain migration in the SRZ, pre-rift basement  
50 fabrics acted as: 1) zones of mechanical strength contrast that localized the large rift faults,  
51 and 2) mechanical 'barriers' that refracted and possibly, temporarily halted the propagation  
52 of the rift zone. Further, the cooled RP1-RP2 mafic dikes facilitated later-phase deformation  
53 in the form of border fault hard-linking transverse faults that exploited mechanical  
54 anisotropies within the dike clusters and served as mechanically-strong zones that arrested  
55 some of the RP3 fault-tips. Overall, we argue that during pulsed rift propagation, inherited  
56 strength anisotropies can serve as both strain-localizing, refracting, and transient strain-  
57 inhibiting tectonic structures.

58

59 *Keywords:* Continental extension, Multiphase rifting, Strain localization, Strain migration,  
60 Structural inheritance

61 **1 INTRODUCTION**

62 The extensional deformation and break-up of the continental lithosphere often occur  
63 over multiple phases of stretching (Keep and McClay, 1997; Bergh et al., 2007; Mohriak and  
64 Leroy, 2013; Bell et al., 2014; Phillips et al., 2019a). Multiphase rifts may experience a  
65 rotation in extension direction between the different phases, leading to the geometrical  
66 modification of the earlier-established fault systems (Duffy et al., 2017; Bell et al., 2014;  
67 Henstra et al., 2015). Also, multiphase rifts commonly show evidence of complex patterns of  
68 spatial migration of strain and depocenters between the different phases, associated with  
69 the abandonment and later reactivation of the early rift faults, and/or creation of new fault  
70 systems (Ebinger et al., 2000; Bell et al., 2014; Brune et al., 2014; Ford et al., 2017; Fazlikhani  
71 et al., 2020). These processes facilitate the overall progressive growth of multiphase rift  
72 basins by the deepening, lengthening, and/or widening of the basin, demonstrated by an  
73 increase in the extent of the deformation.

74 As continental extension initiates, rift basins may attain significant width and length  
75 during the earliest phase of extension (e.g., Modisi et al., 2000; Rotevatn et al., 2018) and  
76 crustal strength properties may influence the lateral propagation of the rift tip (Van Wijk and  
77 Blackman, 2005). However, the recurrence of extension with prolonged inter-rift periods or  
78 decreased stretching rates could heal the mantle-lithosphere, and facilitate depocenter  
79 abandonment and migration of strain to an outboard zone of unrifted crust (e.g., Braun,  
80 1992; Naliboff and Buitier, 2015). This outward migration of the crustal deformation leads to  
81 a progressive enlargement of the brittle deformation field, with associated crustal  
82 subsidence and rift-related sedimentary and/or volcanoclastic accumulation (Mohriak and  
83 Leroy, 2013; Naliboff and Buitier, 2015; Ford et al., 2017; Gawthorpe & Leeder, 2000).

84 Here, we examine the longstanding question of how evolving continental rifts  
85 propagate over multiple phases of tectonic extension, especially in the case of juvenile  
86 (stretching stage; low beta factor) rift settings. We explore this problem in the Shire Rift Zone  
87 (SRZ), East Africa (Figure 1a), which is one of the basins that experienced all the known  
88 phases of Phanerozoic extensional tectonics that affected the region. The NW-trending SRZ  
89 is located between the southern tip of the Malawi Rift, the Lower Zambezi Rift, and Urema  
90 Graben, and extends

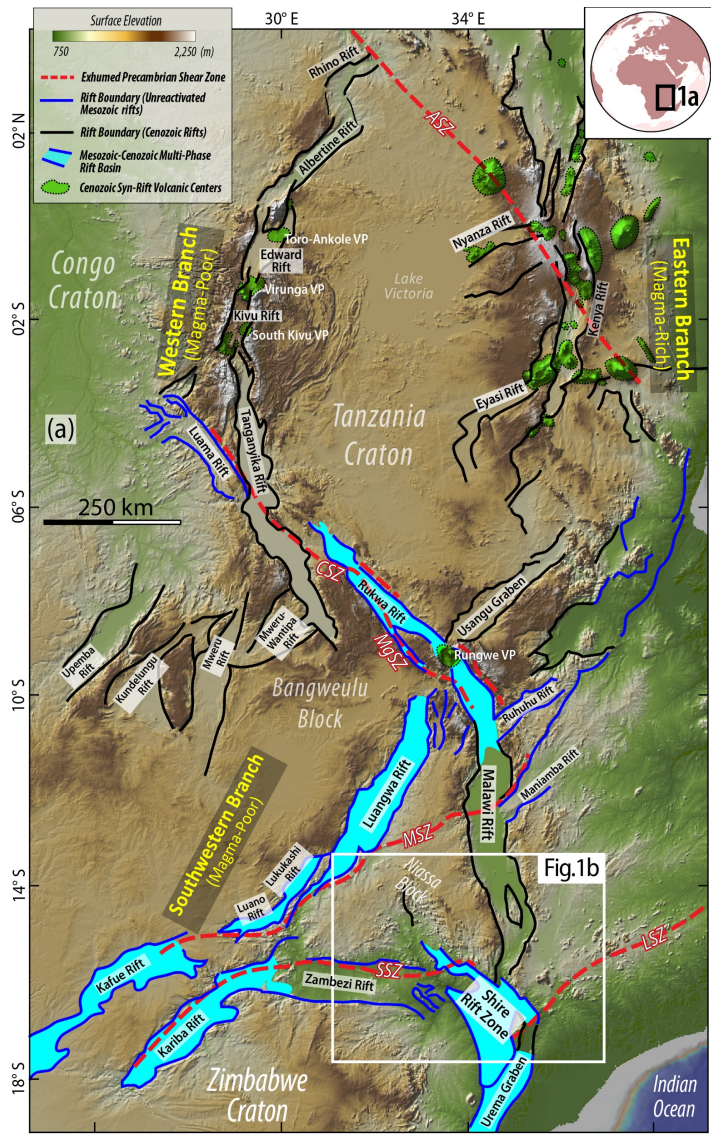
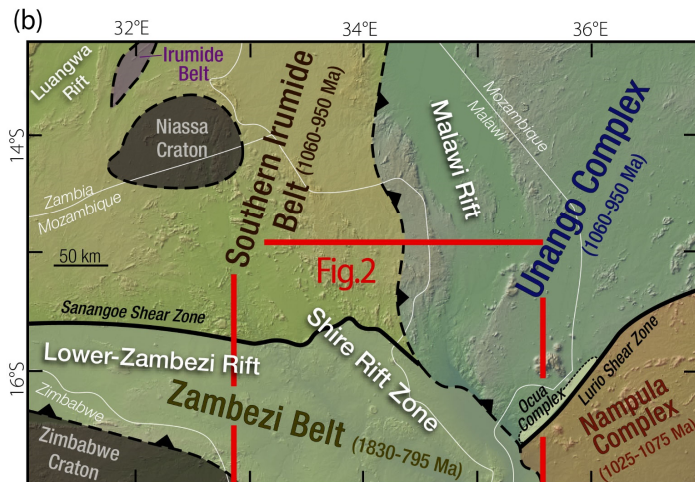


**Figure 1. Regional tectonic setting.** (a) Global Multi-resolution Topography (GMRT) digital elevation model (DEM) hillshade map of Eastern Africa showing the various segments of the East African Rift, and major Precambrian basement shear zones in the region (modified after Daly et al., 1989, Castaing, 1991; Delvaux, 1989; Fritz et al., 2013; Heilman et al., 2019). ASZ: Aswa Shear Zone, CSZ: Chisi Suture Zone, LSZ: Lurio Shear Zone, MgSZ: Mughese Shear Zone, MSZ: Mwembeshi Shear Zone, SSZ: Sanangoè Shear Zone. The blue polygons extend across rift segments with records of multiphase (Mesozoic-Cenozoic) extension and are not indicative of the part of the rift that was active during a particular phase of extension. GMRT source: Ryan et al. (2009). The GMRT base map is obtained from GeoMapApp. (b) Generalized map of the Precambrian basement terranes in the region of the Shire Rift (modified after Hargrove et al., 2003; Westerhof et al., 2008; Fritz et al., 2013). Although there is no clearly defined single shear zone separating some of the tectonic blocks (as indicated by dashed black lines), the Sanangoe and Lurio shear zone terrane boundaries are well defined and constrained in field studies (Barr and Brown, 1987; Bingen et al., 2009). Sawtooth pattern on dashed lines indicates thrust relationship between the flanking terranes or basement blocks (after Westerhof et al., 2008).



135 across the political boundaries of Malawi and Mozambique (Figure 1b). The rift zone, which  
136 developed within an exhumed Precambrian metamorphic crystalline basement (Figure 2),  
137 exhibits excellent surface exposure of rift fault escarpments (Figure 3a), the pre-rift intra-  
138 basement fabrics along the rift margins (Figures 3b-c), and multiphase syn-rift sedimentary  
139 sequences within the rift basin and hanging walls of the rift-bounding faults (Figures 3a, 3d-  
140 e).

141 We integrate field structural measurements, aeromagnetic data, digital elevation  
142 model (DEM) hillshade maps, and published field and borehole data to investigate  
143 multiphase rifting in the SRZ. Our study presents an updated structure of the rift zone,  
144 highlighting the patterns of strain migration and how the rift transitioned from magma-rich  
145 rifting into magma-poor rifting over three phases of tectonic extension. Also, the study  
146 presents evidence suggesting that pre-rift crustal structures (and those inherited in earlier  
147 rift phases) may influence rift evolution by playing the contrasting roles of 1.) weak,  
148 exploitable structures that promote strain localization, and 2.) resisting structures that  
149 transiently arrest or refract the lateral propagation of rift segments and associated faults.

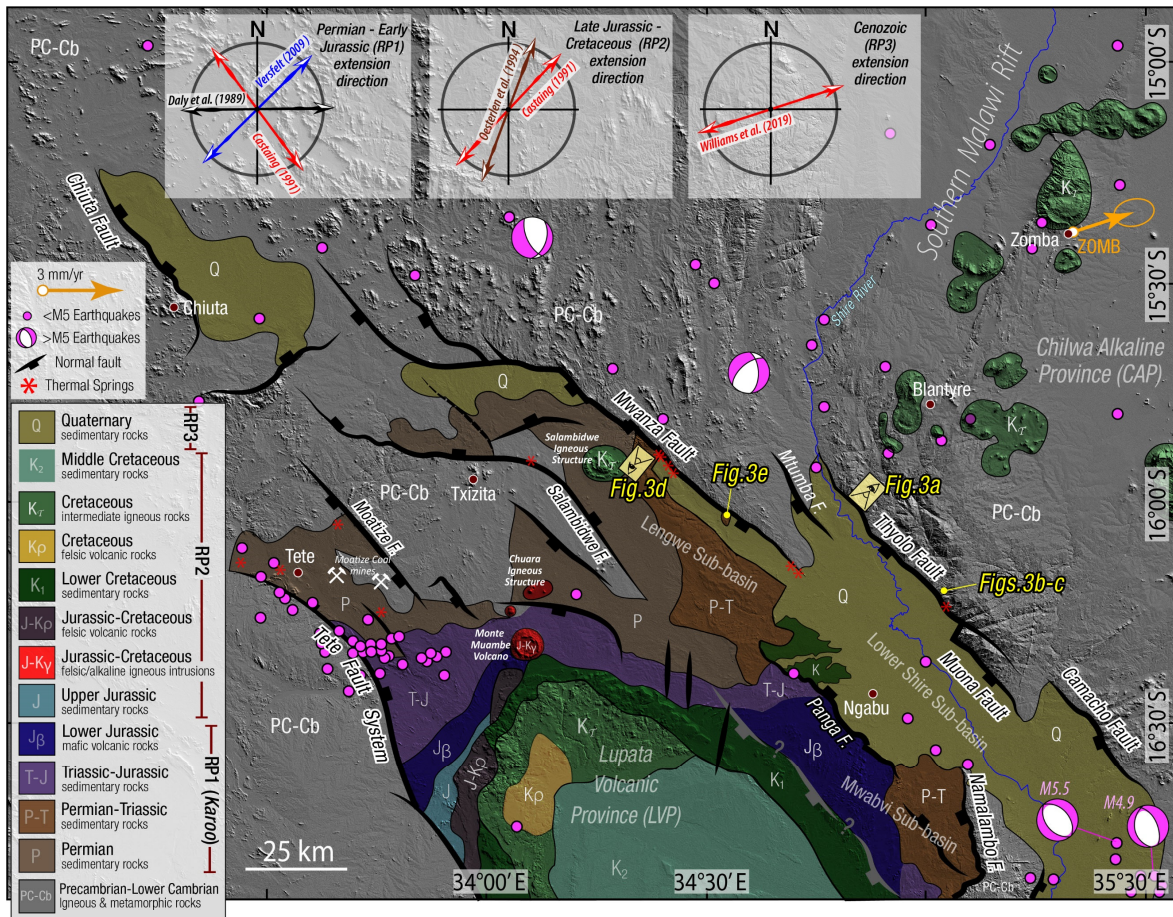
150

## 151 **2 GEOLOGICAL SETTING**

152 Eastern Africa has experienced multiple phases of extensional tectonic deformation  
153 in the Phanerozoic Eon (e.g., Delvaux, 1989; Castaing, 1991; Chorowicz, 2005). These rifting  
154 phases include the Permian – Early Jurassic (Karoo) rifting event herein referred to as rift-  
155 phase 1 (RP1), a Late Jurassic - Cretaceous rifting event (rift-phase 2, RP2), and the current  
156 Cenozoic phase of tectonic extension known as the ‘East African Rift System’ (rift-phase 3,  
157 RP3). Some of the RP1 basins, among which is the SRZ, were reactivated during RP2, and  
158 again reactivated in RP3 (Figure 1a; Delvaux, 1989; Castaing, 1991; Daly et al., 2020). The  
159 SRZ is a NW-trending rift basin, flanked to the north by the N-trending Malawi Rift, to the  
160 west by the E-trending Zambezi Rift, and to the south by the NNE-trending Urema Graben  
161 (Figure 1a). Although the SRZ has been included as part of the Malawi Rift in some older  
162 literature (e.g., Ebinger et al., 1987), following Castaing (1991), we distinguish the SRZ and  
163 its sub-basins based on the distinct NW-SE trend of their border faults, onlapping syn-rift  
164 sequences, and the basement-highs at the zones of interaction between the rifts (Kolawole

165 et al., 2021b). Each of the flanking rift segments, excluding the Urema Graben, are separated  
 166 from the SRZ by a zone of exposed or shallowly-buried pre-rift basement, distinguishing the  
 167 SRZ as a distinct tectonic element in the region (Castaing, 1991; Kolawole et al., 2021b).

168  
 169  
 170  
 171  
 172  
 173  
 174  
 175  
 176  
 177  
 178  
 179  
 180  
 181  
 182  
 183  
 184  
 185  
 186



187  
 188 **Figure 2. Geologic setting of the Shire Rift Zone.** (a) Geologic Map of the Shire Rift Zone overlaid on Shuttle  
 189 Radar Topography Mission (SRTM) digital elevation model. The map is compiled from Cooper and Bloomfield  
 190 (1961), Habgood et al. (1963), Habgood (1973), Choubert et al., (1988), Bennett (1989), Castaing (1991),  
 191 Chisenga et al. (2018), Nyalugwe et al. (2019a). *Top insets* show the inferred RP1 and RP2 regional extension  
 192 directions from previous studies (Daly et al., 1989; Castaing, 1991; Oesterlen and Blenkinsop, 1994; Versfelt,  
 193 2009). The RP3 regional extension direction (Williams et al., 2019) was calculated from earthquake focal  
 194 mechanism inversion. The orange arrow (ZOMB) represents the RP3 GNSS vector and velocity solution (with  
 195 95% uncertainty ellipse) for southern Malawi, from Stamps et al. (2018). Thermal springs are from Procesi et  
 196 al. (2015), Njinju et al. (2019b), and Addison et al. (2021). Earthquakes are compiled from United States  
 197 Geological Survey earthquake catalog, Williams et al. (2019), and Stevens et al. (2021). Note that seismicity in  
 198 the Tete region is associated with coal mining operations in the Moatize coal mines Stevens et al. (2021).

199  
 200

## 201 **2.1 The Pre-Rift Precambrian Basement**

202 The SRZ extends along the tectonic boundaries separating four distinct Precambrian  
203 mobile belts and terranes (Figure 1b), which include the Southern Irumide Belt (1060 - 950  
204 Ma), Zambezi Belt (1830 - 795 Ma), the Unango Complex (1060 - 950 Ma), and the Nampula  
205 Complex (1025-1075 Ma) (Hargrove et al 2003; Fritz et al., 2013). These mobile belts are  
206 composed of Paleoproterozoic-Mesoproterozoic crust which has been reworked and  
207 overprinted by contractional structures and igneous intrusions of the Neoproterozoic Pan  
208 African Orogeny. Overall, the mobile belts are dominated by schists, amphibolite and  
209 granulitic gneisses, and deformed granites, granodiorites, syenites, gabbro, and anorthosites  
210 (e.g., Figures 3b-c; Barr and Brown, 1987; Fritz et al., 2013).

211 Several field studies have revealed the presence of prominent crustal- and  
212 lithospheric-scale shear zones and sutures separating these basement terranes. These shear  
213 zones include the E- to ENE-trending Sanangoe Shear Zone (SSZ) separating the Southern  
214 Irumide Belt and Zambezi Belt (e.g., Barr and Brown, 1987; Kröner et al., 1997; Evans et al.,  
215 1999; Westerhof et al., 2008), and the NE-trending Lurio Shear Zone (LSZ) (Bingen et al.,  
216 2009; Sacchi et al., 2000; Westerhof et al., 2008) which defines the boundary between the  
217 Unango and Nampula Complexes (Figures 1a-b). The SSZ deformation is a 3 - 8 km wide zone  
218 of thrust duplexes and associated cataclasites (Barr and Brown, 1987), defining a crustal-  
219 scale south-dipping thrust boundary between two Proterozoic basement terranes: 1) the  
220 Tete Province to the south, within which the E- to ENE-trending gneisses, pelitic schists, and  
221 quartzites have been pervasively intruded by gabbroic plutons and anorthosites of the Tete  
222 Complex, and 2) the Luia Group Terrane to the north, which hosts gneisses, granulites and  
223 Charnockites (Barr and Brown, 1987; Evans et al., 1999). Based on the regional clustering  
224 patterns of deformed Proterozoic and Mesozoic alkaline rocks and carbonatites, it was  
225 inferred that the SRZ exploited a Late Proterozoic suture zone (Burke et al., 2003).

226

## 227 **2.2 Multiphase Phanerozoic Rifting**

228 The SRZ, which extends ~264 km along-strike and ~134 km in width (maximum  
229 width in the southeast), is defined by an area of fault-bounded syn-rift sedimentary and  
230 volcanoclastic sequences (Figure 2). The rift zone has undergone three distinct phases of

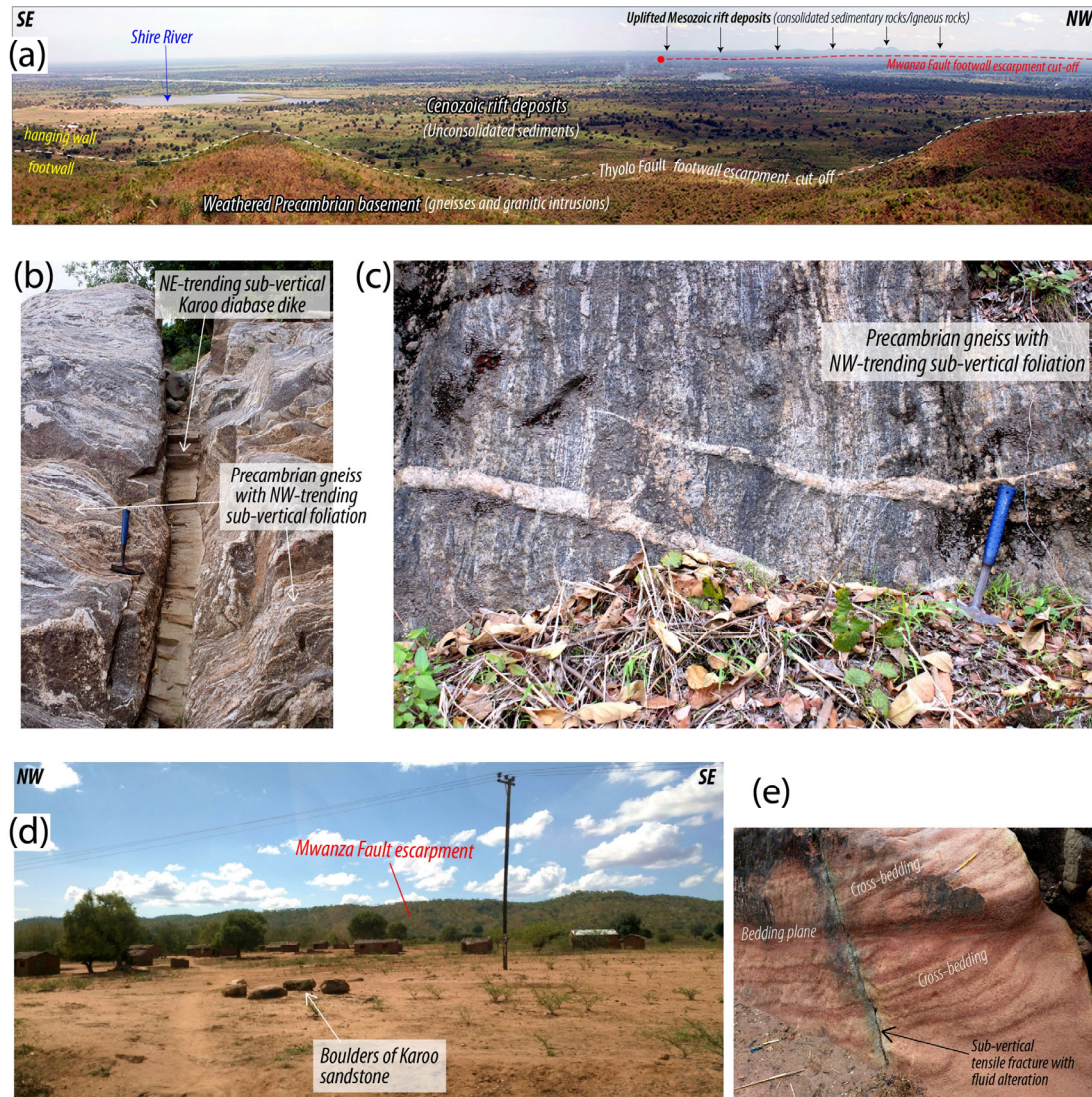


**Figure 3.** (a) Landscape photograph overlooking the Lower Shire River valley of the Shire Rift, looking southwest from the top of the Thyola Fault escarpment (see location in Figure 2a). (b - c) Outcrops of Precambrian gneissic basement along the footwall of the Thyola Fault showing NW-trending sub-vertical foliation. In Figure 3c, a sub-vertical NE-trending Jurassic diabase dike crosscuts the metamorphic foliation of the Precambrian gneiss host rock. (d) Landscape photograph looking northeast from the hanging wall of the Mwanza Fault. (e) Photograph of Karoo sandstone outcrop in the hanging wall of the Mwanza Fault. Also, see the locations of Figures 3b-e in Figure 2.

extension in post-Precambrian times (Figure 2; Castaing, 1991). The first episode of rifting (RP1), popularly known as the “Karoo” rifting episode, began in the Permian and ended in the Lower Jurassic (Castaing, 1991; Delvaux, 1989). This initial phase of extension established large >150 km-long basin-bounding master faults (border faults) which include

263 the SW-dipping Mwanza and Namalambo Faults to the northeast and a NE-dipping fault  
264 system (herein referred to as the ‘Tete Fault System’) to the southwest (Figure 2; Castaing,  
265 1991). The early phase syn-rift fill is dominated by sedimentary sequences deposited in sub-  
266 basins defined by grabens and half grabens (Figures 2, 3d-e; Habgood, 1963; Choubert et al.,  
267 1988; Castaing, 1991). Among these RP1 sub-basins, only the Lengwe and Mwabvi domains  
268 have been studied in detail due to the widespread outcrops of the syn-rift units in Southern  
269 Malawi (Figure 2; Habgood, 1963; Castaing, 1991). RP1 was concluded by the emplacement  
270 of igneous centers and diabase dike swarms across the basin in the Early Jurassic, known as  
271 the Stormberg vulcanicity (e.g., diabase dike in Figure 3b; Habgood et al., 1963, 1973;  
272 Woolley et al., 1979). Studies of RP1 rifting in the region inferred contrasting orientations of  
273 regional extension direction (Figure 2 insets). Versfelt (2009) and Daly et al. (1989, 1991)  
274 proposed an E- to NE-extension direction, based on a broad kinematic interpretation of  
275 regional transtension driven by north-directed far-field compression from the south during  
276 the Gondwanide Orogeny (Daly et al., 1991; Trouw and De Wit, 1999). Whereas Castaing  
277 (1991) inferred a NW-extension direction, based on the presence of NE-trending Late RP1  
278 Stormberg dike swarm in the Shire Rift Zone, assuming a dike-orthogonal dilatant opening  
279 direction (e.g., Fig. 3b).

280 The second phase of extension (RP2) was relatively short-lived, occurring between  
281 the Middle Jurassic and the Cretaceous (Castaing, 1991). RP2 extension was associated with  
282 the reactivation of the RP1 faults, voluminous expulsion of volcanic material and relatively  
283 minor clastic deposition and are well-documented in the southwestern (Lupata Volcanic  
284 Province, LVP), southeastern (Mwabvi sub-basin), and northeastern parts of the basin  
285 (Salambidwe Igneous Structure in the Lengwe sub-basin) (Castaing, 1991; Choubert et al.,  
286 1988). The magmatic activities also extended into areas outboard of the basin, particularly  
287 the Chilwa Alkaline Province (CAP; Figure 2; Cooper and Bloomfield, 1961; Nyalugwe et al.,  
288 2019a). The Cretaceous-age dikes are alkaline in composition with a set trending NE and  
289 another set trending NW (Castaing (1991). Although the stress inversion of slickenside  
290 striations obtained along major faults in the Lengwe and Mwabvi sub-basins show a ‘post-  
291 Karoo’ NE-SW mean extension direction, assuming a dike-orthogonal dilatant opening  
292 direction, Castaing (1991) proposed an initial minor NW-extension, but dominant NE-

293 extension direction for RP2. Based on strain analysis of slickenside striations and fault plane  
294 orientations in Late RP1 and RP2 syn-rift units within the nearby Zambezi Rift (see Fig. 1a),  
295 Oosterlen and Blenkinsop (1994) inferred an NNE-regional extension direction.

296 The third phase of extension (RP3) is associated with the currently active East African  
297 Rift System. In the region of the SRZ, RP3 is thought to have begun in the Late Tertiary  
298 (Delvaux, 1989) or Quaternary (Castaing, 1991), and is associated with localized deposition  
299 of Quaternary sediments in the Lower Shire Valley of southern Malawi (Figures 2 and 3a;  
300 Castaing, 1991; Chisenga et al., 2019) and the Chiuta area of Mozambique (Figure 2;  
301 Choubert et al., 1988; Castaing, 1991). Although the RP1 and RP2 tectonic extension in the  
302 SRZ were associated with widespread volcanism (magma-rich rifting), RP3 is non-magmatic.  
303 The Quaternary Lower Shire depocenter (also known as “Shire Graben” or “Lower Shire  
304 Graben”) is bounded to the east by a system of SW-dipping normal faults which consist of  
305 the Thyolo (Figure 3a), Muona, and Camacho Faults, and to the west by the Panga Fault  
306 (Figure 2). The Panga Fault is interpreted to have initially developed within the hanging wall  
307 of the Mwanza border fault during RP1 but had been reactivated in post-RP1 times marked  
308 by the brecciation of a Late RP1 dolerite dike contained within the fault zone (Habgood,  
309 1963; Castaing, 1991). In the Chiuta area, which is the northwesternmost sub-basin in the  
310 SRZ, the west-bounding fault, herein referred to as “the Chiuta Fault”, represents the border  
311 fault in this part of the rift zone (Figure 2).

312 The SRZ exhibits a thinned lithosphere and elevated heat flow relative to the rift  
313 flanks (Njinju et al., 2019a, 2019b). The RP3 regional extension direction is ENE- to E-W and  
314 is responsible for several recent >Mw4 earthquakes in the basin (Figure 2; Williams et al.,  
315 2019). Geodetic velocity solutions for the region show strain rates of ~2.2 mm/yr (Figure 2;  
316 Stamps et al., 2018; Wedmore et al., 2021), and a geomechanical analysis shows that the RP3  
317 eastern border faults are favorably oriented for reactivation in the regional stress field  
318 (Williams et al., 2019). Although the broad geologic history of the SRZ has been identified in  
319 previous studies (Habgood, 1963; Castaing, 1991), the major structural domains and  
320 associated structural elements, the patterns of strain localization and migration, and  
321 mechanics of rift propagation over its multiphase history remain unknown.

322

323 **3 DATA AND METHODS**

324 We integrated field observations from this study and previous studies, digital  
325 elevation model (DEM) hillshade maps, intra-basinal borehole penetration logs, and  
326 aeromagnetic data to generate an updated tectonic and structural framework for the SRZ,  
327 allowing us to evaluate its multiphase rifting history.

328 To create an updated geologic map of the SRZ, we compile published geological maps  
329 (Cooper and Bloomfield, 1961; Habgood, 1973; Habgood et al., 1963; Choubert et al., 1988),  
330 which document field observations of the surficial geology across the rift basin and  
331 surrounding areas. The compilation allows us to constrain the rift-related lithological units  
332 and the spatial extents of the sub-aerial exposures and locations of juxtaposition against the  
333 Precambrian basement. We integrated the published legacy geologic maps with subsurface  
334 data from borehole penetrations (where available in the basin) and observations from  
335 aeromagnetic fabric patterns beneath the rift basin deposits.

336 To provide an updated fault map of the rift zone, we first compiled fault lineaments  
337 from the legacy geologic maps and previous studies in various parts of the rift (Choubert et  
338 al., 1988; Castaing, 1991; Chisenga et al., 2018; Wedmore et al., 2020). These previous  
339 studies mostly mapped faults from surface topographic scarps and outcrops but lack  
340 information on the buried fault segments. Also, the mapping of potential buried faults from  
341 linear gradients in a bouguer gravity grid covering the Malawi part of the basin (Chisenga et  
342 al., 2018) is subject to the low resolution of the gravity data and lacks geological constraints.  
343 To update the fault maps, we delineated additional fault segments using the vertical  
344 derivative of the available aeromagnetic grids across the basin (Figures S1a-c). Although our  
345 fault mapping mostly consists of buried faults and buried extensions of exposed faults  
346 interpreted from filtered aeromagnetic maps, we also interpreted additional surface-  
347 breaking fault segments from topographic hillshade maps (see Figure S2). Below, we provide  
348 the details of the field data collection, borehole data, and aeromagnetic datasets, and data  
349 analysis techniques used in the study.

350

351

352

### 353 **3.1 Field Data**

354 We conducted a field campaign in the Malawi part of the SRZ, covering the footwall  
355 and hangingwall areas of the Thyolo-Muona and Mwanza border fault systems (Figures 3a-  
356 e). In the exposures of the pre-rift gneissic basement along the footwalls of the rift border  
357 faults, we collected field measurements of the strike and dip of the metamorphic basement  
358 fabrics (i.e. foliation; n=39 along Mwanza Fault's footwall, and n=229 along Thyolo-Muona  
359 Fault's footwall). Along the footwall of the Thyolo-Muona Fault, where Mesozoic diabase dike  
360 intrusions are ubiquitous across the basement (e.g., Figure 3b), we collected field  
361 measurements of the strike and dip of the dikes where possible (n=50). We present the 3-  
362 dimensional (3D) structural datasets as equal-area stereographic projections of poles to  
363 planes with 2-interval Kamb contours. We augment our field measurements along the  
364 Thyolo-Muona Fault's footwall with datasets previously collected by the Geological Survey  
365 of Malawi and published in Habgood et al. (1973). The Geological Survey of Malawi structural  
366 dataset consists of strike/dip of gneissic foliation (n=191), and map-view traces of diabase  
367 dikes which we digitized and from which we automatically extracted 2,086 strike  
368 measurements of dike segments using ArcMap.

369

### 370 **3.2 Shuttle Radar Topography Mission (SRTM) Digital Elevation Model (DEM)**

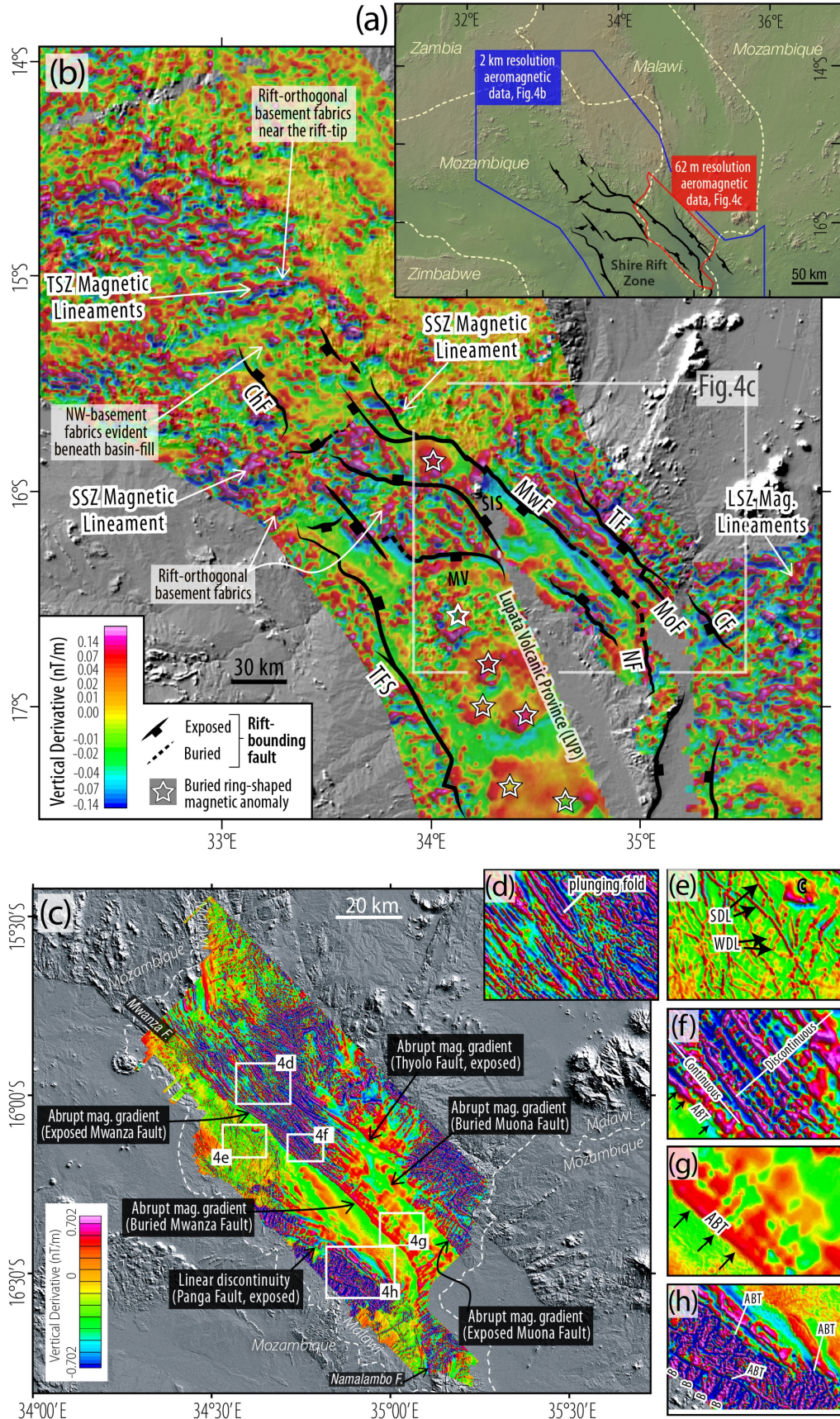
371 In the less-studied sub-basins of the Shire Rift Zone, in combination with  
372 aeromagnetic data (see section 3.5), we utilized 1 arc-second (30 m spatial resolution)  
373 Shuttle Radar Topography Mission (SRTM) DEM hillshade maps to delineate surface traces  
374 of normal faults. In areas where the aeromagnetic data used in this study is of lower  
375 resolution (e.g., NW and SE termination zones of Shire Rift), we mapped the topographic  
376 lineaments in the DEM hillshade maps of basement exposures as supporting independent  
377 data on the trends of the basement metamorphic fabrics.

378

### 379 **3.3 Aeromagnetic Data**

380 For the mapping of buried fault segments, dikes, and buried volcanic centers, and the  
381 modeling of the depth-to-magnetic basement, we utilize two aeromagnetic datasets: a lower  
382 resolution (2 km spatial resolution) regional grid covering the entire basin (both the Malawi

383  
384  
385  
386  
387  
388  
389  
390  
391  
392  
393  
394  
395  
396  
397  
398  
399  
400  
401  
402  
403  
404  
405  
406  
407  
408  
409



410 **Figure 4. Aeromagnetic datasets.** (a) Regional hillshade topography map (same as Fig. 1b) showing the  
 411 coverage of the aeromagnetic datasets used in the study. (b) 1<sup>st</sup> vertical derivative of the regional-scale pole-  
 412 reduced aeromagnetic grid (2 km spatial resolution) covering the Shire Rift and surrounding areas. CF:  
 413 Camacho Fault, ChF: Chiuta Fault, LSZ: Lurio Shear Zones, MoF: Muona Fault, MV: Monte Muambe Volcano,  
 414 MwF: Mwanza Fault, NF: Namalambo Fault, SIS: Salambidwe Igneous Structure, SSZ: Sanangoe Shear Zones,  
 415 TSZ: Techigoma Shear Zone. The delineation of the shear zones (LSZ and SSZ) is constrained by field  
 416 observations in Barr and Brown (1987); Sacchi et al. (2000), Kroner et al. (1997), Bingen et al. (2009), Fritz et  
 417 al. (2013). (c) 1<sup>st</sup> vertical derivative of the higher-resolution pole-reduced aeromagnetic grid (62 m spatial  
 418 resolution) covering only the Malawi part of the rift basin. Salient aeromagnetic fabric patterns observable in  
 419 the high-resolution aeromagnetic map include: (d) Broad clusters of parallel, elongate magnetic fabrics in the  
 420 exposed basement (i.e. basement metamorphic foliation). (e) Cross-cutting discrete magnetic-high lineaments  
 421 enclosed by magnetic-low anomalies (i.e. mafic igneous dikes in sedimentary strata). 'SDL': Strong discrete  
 422 lineament (shallow dike), 'WDL': Weak discrete lineament (deep-seated dike), 'C': Discrete magnetic-high ring-  
 423 shaped anomaly (ring intrusion or sill?). (f) Mesh pattern fabrics in the exposed basement (i.e. metamorphic  
 424 foliation overprinted by cross-cutting mafic dikes). (g) Mesh pattern fabrics in the buried basement (i.e. buried  
 425 part of the basement exposed in Figure 3f). (h) Compact linear bands of chaotic magnetic fabrics (i.e. exposed  
 426 or shallowly buried mafic volcanic deposits). The fabric becomes diffused northeastward as the depth of burial  
 427 of the volcanic flows increases. 'B': compact band, 'ABT': abrupt magnetic gradient (i.e. normal fault). See  
 428 Figures S1a-c for unfiltered and uninterpreted versions of the aeromagnetic grids. The unfiltered total magnetic  
 429 intensity grids of these vertical derivative maps are in supplementary figures S1a-c.

430

431

432 and Mozambique sections) and surrounding areas (Figures S1a-b, 4a-b), and a higher  
 433 resolution (62 m spatial resolution) grid covering only the Malawi section of the basin  
 434 (Figures S1c, 4a, and 4c). The regional dataset (Figure S1a) consists of a grid of merged  
 435 aeromagnetic field data acquired in the 1970s and 1980s from countries in southern Africa  
 436 (source: South Africa Development Community, SADC aeromagnetic data, provided by  
 437 Council for Geoscience, South Africa). This regional data includes a legacy Malawi  
 438 aeromagnetic grid which has a resolution of ~250 m spatial resolution and was acquired in  
 439 1984/1985 with a 120 m terrane clearance and 1 km-spaced NE-SW flight lines (Figure S1b;  
 440 Kolawole et al., 2018). The 62 m-resolution Malawi aeromagnetic data (Figure S1c) was  
 441 acquired in 2013 (source: Geological Survey Department of Malawi; Nyalugwe et al., 2019b)  
 442 with 80 m terrane clearance along NE-SW lines with a line spacing of 250 m.

443

### 444 **3.4 Borehole Data**

445 To investigate the subsurface stratigraphy in the RP3 Lower Shire Sub-basin, we  
 446 assessed available lithologic logs from borehole penetrations below the Quaternary  
 447 sediments, which are documented in Habgood (1963) and Habgood et al. (1973) (Figure S3a-  
 448 b). There is no known documentation of well penetration beneath the Quaternary sediments

449 in the RP3 Chiuta Sub-basin. Therefore, to infer the dominant basin fill of the Chiuta Sub-  
450 basin, we relied on published surficial geologic maps, aeromagnetic fabric analysis, and  
451 lateral variations in DEM hillshade surface roughness patterns across the sub-basin.

452

### 453 **3.5 Structural Interpretation from Aeromagnetic Data**

454 Although structural deformation is commonly expressed as ‘abrupt’ gradients in  
455 aeromagnetic grids, the distinct magnetic character and expressions of basement-rooted  
456 fault traces, cross-cutting mafic dike intrusions, dike-intruded fault zones, and exhumed  
457 metamorphic terrane fabrics can be distinguished (Jones-Cecil et al., 1995; Modisi et al.,  
458 2000; Kinabo et al., 2007, 2008; Grauch & Hudson, 2007; Kolawole et al., 2018; 2017;  
459 Heilman et al., 2019). The total magnetic intensity (TMI) aeromagnetic data is a grid of  
460 magnetic anomalies produced by a combination of the magnetic susceptibility of the sources,  
461 the depth to the top of the magnetic sources, and the steepness of the contacts between  
462 distinct magnetic bodies [e.g., Grauch & Hudson, 2007, 2011]. However, due to the vertical  
463 offset and lateral juxtaposition of layers of strongly contrasting magnetic properties across  
464 steep fault planes, derivative-filtered aeromagnetic grids can resolve both buried and  
465 surface-breaking normal faults that offset the primary magnetic units. Similarly, the lateral  
466 alternation of mafic and felsic mineral banding in gneissic rocks (metamorphic basement  
467 fabrics), and mafic dikes cross-cutting gneissic basement are resolvable by derivative  
468 aeromagnetic grids which allows the delineation of their large-scale trends (Kinabo et al.,  
469 2007, 2008; Kolawole et al., 2018; Heilman et al., 2019; Lemna et al., 2019). Thus, the  
470 aeromagnetic datasets covering the SRZ allow us to delineate the rift-related faults (sub-  
471 aerial and subsurface), buried and sub-aerial magmatic structures (dikes and ring-shaped  
472 intrusions), and pre-rift basement fabrics within the Shire Rift and along its margins.

473 However, before structural interpretation, we first pole-reduced (RTP) the total  
474 magnetic intensity (TMI) aeromagnetic datasets to correct for the skewness of the magnetic  
475 field due to the proximity of the study area to the equator (Baranov, 1957; Arkani-Hamed,  
476 1988). Here, we preferred RTP correction over equator-reduction (RTE) because the RTP  
477 correction produced a grid with better alignment of fault-related gradients with their  
478 geologic sources in areas where the surface breaking fault traces provide geologic

479 constraints (see Kolawole et al., 2018). After RTP correction, we applied a vertical derivative  
480 filter to the TMI-RTP data to better resolve the structure-related gradients in the grids  
481 (Figures 4b-h) (e.g., Ma et al., 2012; Kolawole et al., 2017; 2018; Heilman et al., 2019).  
482 Following a systematic characterization of the aeromagnetic patterns observable in the 2013  
483 Malawi aeromagnetic grid (Figures 4d-4h), we identified distinct patterns herein referred to  
484 as ‘aeromagnetic facies’, which allow a better interpretation of the structural character of the  
485 associated magnetic sources. To assess the orientation of basement foliation and mafic dikes  
486 in the SRZ, independent of the collected field measurements (see section 3.1), we digitized  
487 and measured the trend of the aeromagnetic anomaly lineaments corresponding to the  
488 structures constrained by published geologic map of the basement structures (Habgood et  
489 al., 1973). In the Mozambique part of the SRZ where a lower-resolution aeromagnetic data  
490 is available (Figure S1), we supplemented aeromagnetic mapping with the digitization and  
491 trend measurement of topographic lineaments representing basement fabrics.

492 Further, we calculated the frequency-azimuth distribution of the measured lineament  
493 trends within the relevant segments of the rift zone. For multimodal distributions, we  
494 divided the data into their modal sets using the frequency minima. For both unimodal and  
495 multimodal plots, we calculated the circular vector mean and 95 % confidence interval for  
496 the modal sets using the method of Mardia and Jupp (2009). Note that the magnitude of the  
497 confidence interval is dependent on the number of sample data used. All frequency-azimuth  
498 plots present in this study are area-weighted.

499

### 500 **3.6 Estimation of Depth-to-Magnetic Basement**

501 Along the SRZ, we estimated the depth-to-magnetic basement in two sub-basins  
502 where a widespread accumulation of Quaternary-age sediments is most widespread and  
503 prominent. These sub-basins are in the Chiuta Fault hanging wall and the Lower Shire  
504 Graben (Thyolo-Muona Fault hanging wall) with extensions into the Mwanza Fault hanging  
505 wall (Figure 2). In the Chiuta area, which is in Mozambique, we utilized the available 2 km-  
506 resolution regional aeromagnetic grid (Figures S1a and 4b). Whereas, in the Lower Shire  
507 Graben, located in Malawi, we utilized the original (unmerged) Malawi part of the legacy  
508 regional grid (Figure S1b). Our preference for the unmerged legacy Malawi aeromagnetic

509 grid for source-depth estimation is due to its moderate resolution and suppression of high-  
510 frequency noise (e.g., related to intra-sedimentary mafic dikes).

511 To perform an automatic calculation of depth-to-the top of the magnetic basement,  
512 we used the Source Parameter Imaging™ (SPI™) transform of the aeromagnetic grid  
513 (Thurston and Smith, 1997; Smith et al., 1998). The SPITM technique assumes a step-type  
514 source model and produces spatially distributed source depth-solutions that are  
515 independent of magnetic declination, inclination, strike, dip, and remanent magnetization.  
516 The transform first computes the tilt derivative, and the total horizontal gradient of the tilt  
517 derivative (local wavenumber, K). For a step source model, the Kmax-1 represents the depth  
518 to the magnetic source where Kmax is the peak value of the local wavenumber based on a  
519 simple Blakely test (Blakely and Simpson, 1986). Following standard practice, to minimize  
520 the noise from shallow sources, we applied a Hanning filter to the K grid before calculating  
521 the source depths. The gridding of the depth solutions assumes a 2-layer model such the SPI  
522 map represents the average depth to the top of the shallowest magnetic basement. Source  
523 depth estimations from aeromagnetic data generally have an accuracy of about  $\pm 20\%$  (Gay,  
524 2009), thus, they provide a coarse approximation of lateral variation of depth to the top of  
525 the magnetic basement beneath the rift sedimentary deposits.

526

## 527 **4 RESULTS**

### 528 **4.1 Structural Compartmentalization of the Shire Rift Zone (SRZ)**

529 The updated fault map of the SRZ (Figure S2), integrated with the existing geologic  
530 map of the basin (Figure 2), provides information on the structure and sub-basinal  
531 compartmentalization of the rift zone. The large-scale rift architecture is defined by a NW-  
532 trending basin that bifurcates northwestwards into two 20-25 km-wide grabens, both of  
533 which are bound by large fault systems (Figure 5a). Based on the distribution and ages of  
534 rift-related sedimentary and volcanoclastic units within the confines of these faults (Figure  
535 2), we identify seven sub-basins (Figure 5b). These sub-basins include five magmatic sub-  
536 basins: Lengwe, Mwabvi, Moatize, Monte-Muambe, and Lupata, which host RP1 and RP2  
537 volcano-sedimentary sequences; and two non-magmatic sub-basins: Lower Shire and Chiuta  
538 where widespread RP3 Quaternary sedimentary cover is localized (Figures 2 and 5b). The

539 Lupata Sub-basin hosts a major Mesozoic volcanic zone, the Lupata Volcanic Province (LVP).  
540 The LVP and the Salambidwe Igneous structure define the main intra-rift igneous zones, and  
541 the Chilwa Alkaline Province (CAP) defines an off-rift syn-rift igneous province.

542 Basin-scale rift-orthogonal topographic profiles (profiles P1 to P3; Figures 5a-b)  
543 show that the most-prominent topographic-highs in the SRZ are the southwestern and  
544 northeastern flanks of the Chiuta Sub-basin, the Salambidwe Igneous Structure, the eastern  
545 flank of the Lengwe Sub-basin, and the eastern flank of the Lower Shire Sub-basin. However,  
546 the escarpment height of the border fault zones (Figures 5c-e) is largest in the southwestern  
547 margin of the Chiuta Sub-basin (~696 m) and in the northeastern margin of the Lower Shire  
548 Sub-basin (~708 m), and smallest in the northern margins of the Lengwe Sub-basin (<200  
549 m) and the southwestern margin of the Lupata Sub-basin (66 m). Along the entire rift, the  
550 border faults with the greatest escarpment height are the Chiuta Fault and the Thyolo-Muona  
551 Fault system.

552 At the northwestern tip of the SRZ (Chiuta Sub-basin), the rift morphology defines a  
553 graben geometry in which the basin asymmetrically tilts gently westwards towards the  
554 Chiuta border fault (profile P1, Figure 5c). At the central part of the rift zone (profile P2,  
555 Figure 5b), the rift morphology highlights the western and eastern rift bifurcations (Moatize  
556 and Lengwe Sub-basins), separated by a basement block, which we herein refer to as 'the  
557 Txizita Horst' (after 'Txizita town' in Figure 2). In the southeast, the SRZ is widest, defined  
558 by a ~134 km-wide basin in which the western and central areas (Lupata and Mwabvi Sub-  
559 basins) are elevated relative to the far eastern areas (Lower Shire Sub-basin) (profile P3,  
560 Figure 5c). Although the Quaternary sediments of the Lower Shire Sub-Basin onlap the  
561 Mesozoic sequences in the Lengwe and Mwabvi Sub-basins, a major boundary between the  
562 Mwabvi and Lower Shire is marked by the NE-dipping Panga Fault such that the Mwabvi is  
563 in the SW and Lower Shire in the NE. The surface morphology of the Lower Shire Sub-basin  
564 reflects a graben morphology in which the basin asymmetrically tilts eastwards towards the  
565 Thyolo-Muona-Camacho border fault system. However, all the aeromagnetic grids over the  
566 Lower Shire Graben (e.g., Figures S1a-c) and depth-to-basement map (see section 4.2.1)  
567 show that this sub-basin is further compartmentalized into a deeper SW section and  
568 shallower NE section by the buried southeastern continuation of the Mwanza Fault



598 MDC: Mulata Dike Cluster, MF: Mwanza Fault, MtF: Moatize Fault, MV: Monte Muambe Volcano, NF: Namalambo  
599 Fault, SF: Salambidwe Fault, SIS: Salambidwe Igneous Structure, TF: Thyolo Fault, TFS: Tete Fault System, TH:  
600 Txizita Horst, TSZ: Techigoma Shear Zone. The location, geometry, and extents of the Lurio and Sanangoe Shear  
601 Zones are after Barr and Brown (1987); Sacchi et al. (2000), Kroner et al. (1997), Bingen et al. (2009), Fritz et  
602 al. (2013). The Techigoma Shear Zone is delineated in this current study based on its character as a distinct  
603 high-amplitude aeromagnetic lineament separating terranes of different fabric trends (Figure 2b), collocated  
604 with satellite-scale, plunging tight folds (inset showing Google Earth map). (b) Map showing the Shire Rift  
605 extents and sub-basin compartmentalization based on fault scarp continuity and published distribution of the  
606 syn-rift sedimentary and volcanic deposits (Figure 2; Choubert et al., 1988). LM: Lake Mbenje, LSV: Lurio Shear  
607 Zone, SSZ: Sanangoe Shear Zone. (c - e) Rift-perpendicular topographic profiles (see Figure 5b for profile  
608 transects).

609

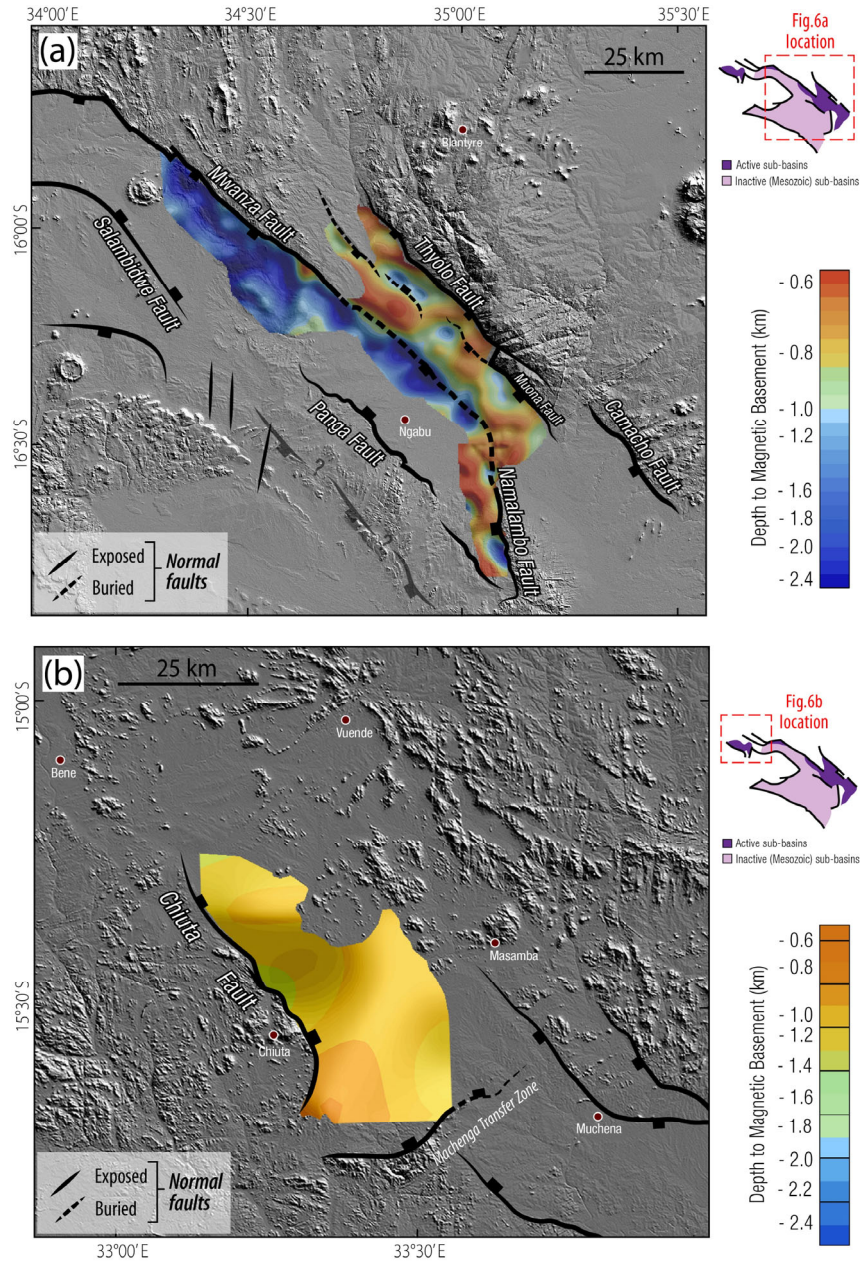
#### 610 *4.2.1 Depth to Magnetic Basement*

##### 611 *The Lower Shire Sub-Basin:*

612 The spatial distribution of depth-to-magnetic basement estimates beneath the Lower  
613 Shire (Figure 6a) shows larger depths in the hanging walls of the Mwanza-Namalambo Fault  
614 System compared to the hanging walls of the Thyolo-Muona Fault System. The results show  
615 that along the Mwanza Fault's hanging wall, the magnetic basement depths range between  
616 ~900 m and 2.4 km and attain a maximum of ~2.7 km at locations within both the exposed  
617 and buried sections of the fault. The hanging wall of the Namalambo Fault exhibits shallower  
618 depths than that of the Mwanza Fault but attains a maximum depth of 2.4 km along its  
619 southern section. Whereas, relative to the Mwanza-Namalambo Fault, the magnetic  
620 basement in the hanging wall of the Thyolo-Muona Fault defines a broad 'shelf' area with  
621 depths mostly ranging between 600 m and 1.2 km but records a maximum of ~1.4 km near  
622 the central areas of the hanging wall.

623 Overall, the hanging wall of the Mwanza Fault features broader and deeper zones of  
624 basement-lows compared to the Thyolo-Muona Fault hanging wall which shows smaller  
625 zones of basement-lows with moderate depths, separated by NW and NE-trending  
626 basement-highs. Thus, although the hanging walls of Mwanza and Thyolo-Muona synthetic  
627 border fault systems are covered by widespread Quaternary syn-rift sedimentary deposits  
628 (Figures 2 and 5e), the subsurface basement structure reveals significant contrast in the  
629 magnitudes of subsidence of the magnetic basement across the border faults.

630  
631  
632  
633  
634  
635  
636  
637  
638  
639  
640  
641  
642  
643  
644  
645  
646  
647  
648  
649



650 **Figure 6. Depth-to-Magnetic Basement in the active (i.e., Cenozoic) Sub-Basins.** (a) Depth-to-magnetic  
651 basement map of the Lower Shire sub-basin (and part of the Lengwe Sub-basin), overlaid on Shuttle Radar  
652 Topography Mission (SRTM) digital elevation model (DEM) hillshade map. The top of RP2 volcanic sequences  
653 is inferred to represent the magnetic basement in the hanging wall of the Mwanza-Namalambo Fault (Domains  
654 1 & 2 in Fig. 7c). Whereas the top of the pre-rift metamorphic basement most likely represents the magnetic  
655 basement to the northeast of the Mwanza Fault (Domains 3-4 in Fig. 7c). (b) Depth-to-magnetic basement map  
656 of the Chiuta sub-basin, overlaid on SRTM-DEM hillshade map. Here, due to a lack of evidence on the presence  
657 of Mesozoic volcanics in this sub-basin, the top of the pre-rift metamorphic basement is inferred to represent  
658 the magnetic basement. Note that the Lower Shire sub-basin depth map shows a higher resolution than that of  
659 the Chiuta sub-basin because of the relatively higher-resolution aeromagnetic data in the Lower Shire sub-  
660 basin (see Figs. 3b-c).

661

662 *The Chiuta Sub-Basin:*

663 The results (Figure 6b) show that the magnetic basement generally deepens  
664 southwestwards towards the Chiuta Fault, attaining a maximum depth of ~1.4 km. To the  
665 southeast, the basement first shallows up to ~1 km before deepening slightly to ~1.2 km  
666 along a NE-trending, NW-dipping fault that terminates the sub-basin against the 'Machenga  
667 Transfer Zone'. Due to the absence of borehole penetration data in the Chiuta sub-basin, the  
668 lateral variation in our depth-to-magnetic basement estimate provides the first insight into  
669 the subsurface structure of the sub-basin.

670

671 *4.2.2 Basement and Stratigraphic Architecture of the Lower Shire Sub-Basin*

672 The Quaternary deposits in the Lower Shire Sub-basin overlap with the Mesozoic syn-  
673 rift deposits of the Lengwe and Mwabvi Sub-basins (Figure 2). Thus, with illustrations in  
674 Figures 7a and 7b, we describe here our observations of the basement and syn-rift  
675 architecture of the Lower Shire Sub-basin relative to those of its bounding sub-basins.

676 The Mwabvi Sub-basin is dominated by RP1 volcano-sedimentary units with no  
677 known accumulation of Quaternary (RP3) sediments (Domain-1 in Figure 7a). The Lengwe  
678 Sub-basin is also dominated by the RP1 units but hosts minor accumulations of RP3  
679 sediments (Figure 2) in the northern segments of the Mwanza Fault (Domain-2 in Figure 7b).  
680 Along the northern Mwanza Fault, the syn-rift sequences are directly juxtaposed against the  
681 Precambrian metamorphic basement exposed in the footwall of the fault (Domain-3 in  
682 Figure 7b). However, towards the southeast, the cover of RP3 sediments in Domain-2 is more  
683 widespread and dominates the surficial extents of the domain.

684 Integration of all available information from independent datasets provides insight  
685 into the syn-rift stratigraphic architecture and lateral variation in the origin of the magnetic  
686 basement across the Lower Shire Sub-basin. These datasets include field observations  
687 (Figures 3a-c), basin-scale surficial geological map compilation (Figure 2), litho-logs from  
688 boreholes that penetrate below the Quaternary sedimentary cover (S3a-b and Table S1), and  
689 aeromagnetic fabric patterns (Figures 4c-h). First, these datasets show that the RP1-RP2  
690 volcano-sedimentary units of the Mwabvi Sub-basin have been faulted and buried beneath  
691 RP3 sediments on the hanging wall of the Panga Fault (Domain-1 and -2 in Figure 7c).

692 Second, borehole logs and the aeromagnetic fabric patterns show that the RP1-RP2 volcanic  
693 rocks do not extend into the footwall of the buried Mwanza Fault segments (Figures 7c, S3a-  
694 b; Table S1). Also, the logs from boreholes in the areas between the Mwanza Fault and Thyolo  
695 Fault show no evidence for the presence of RP1 or RP2 sedimentary rocks beneath  
696 Quaternary sediments as the unconsolidated sediments directly overlie the gneissic  
697 basement (Figure S3a; Table S1). The magnetic structure of the Lengwe Sub-basin where  
698 mafic dikes have intruded the Mesozoic sedimentary sequences (Figure 7b) is different from  
699 that of the hanging wall of the Thyolo-Muona Fault system where high-amplitude anomalies  
700 are sparse and are of long-wavelengths. This suggests that there is no magnetic fabric pattern  
701 defining mafic diking of the sedimentary sequences overlying the gneissic basement in the  
702 hangingwall of the Thyolo Fault (Domain-3 in Figure 7c).

703 Additionally, beneath the Cenozoic cover of the Thyolo-Muona Fault hanging wall, the  
704 aeromagnetic map reveals a long-wavelength, low-frequency gradient that is parallel to- and  
705 extends northeastwards from the NE surface termination of the Muona Fault (Figure 4c). We  
706 describe this gradient as representing a buried (non-surface-breaking) segment of the  
707 Muona Fault. Based on these observations, we present an updated and comprehensive  
708 structural map of the Shire Rift, showing the previously mapped features and those mapped  
709 in this study (Figure 8).

710

#### 711 *4.2.3 Basement and Stratigraphic Architecture of the Chiuta Sub-Basin*

712 The absence of high-resolution aeromagnetic data over the Chiuta Sub-basin does not  
713 permit a detailed structural interpretation. However, a key observation here is that  
714 aeromagnetic lineaments corresponding to a continuation of basement metamorphic fabrics  
715 beneath the rift-fill are visible along the axis of the Chiuta Sub-basin (Figure 4b). This is  
716 consistent with observations in other juvenile rift basins in Eastern Africa where the  
717 shallowly buried metamorphic basement is directly overlain by non-magnetic  
718 unconsolidated sediments (Kinabo et al., 2007; Kolawole et al., 2018),

719

### 720 **4.3 Pre-Rift Basement Metamorphic Fabrics of the Shire Rift Zone (SRZ)**

721 In the areas of exposed basement along the SRZ, aeromagnetic facies representing the  
722 basement metamorphic fabrics (gneissic foliation) are defined by tight clusters of parallel,  
723 elongate magnetic lineaments that show folded geometries along their strike (e.g., Figure  
724 4d). We herein refer to this aeromagnetic pattern as the ‘basement metamorphic fabric’ or  
725 ‘basement fabric’. Also, during our field visit, where possible, we collected strike and dip  
726 measurements of the basement foliation to independently compare with the broader-scale  
727 measurements from aeromagnetic grids. Below, we summarize the results of the frequency-  
728 azimuth distribution of the mapped basement fabrics observed along the SRZ (Figures 9a-g).

729

#### 730 4.3.1 *The Mwanza and Thyolo-Muona Border Faults and Environs*

731 Along the Mwanza Fault, the frequency-azimuth distribution of the basement fabric  
732 (Figure 9bi) shows a dominant NW-SE trend with a  $140^\circ$  mean trend that is sub-parallel to  
733 the fault trend ( $\sim 136^\circ$ ). This is consistent with our field measurements of the basement  
734 foliation (stereographic projection inset in Figure 9bi). Along the Thyolo-Muona Fault  
735 system, the mapped aeromagnetic metamorphic fabrics also show a prominent NW-SE trend  
736 with a mean of  $123^\circ$  (Figure 9ci), which is consistent with field measurements ( $128^\circ$ ), both  
737 being parallel or sub-parallel to the fault trend ( $\sim 131^\circ$ ). We also note that along both the  
738 Mwanza and Thyolo Faults, the average dip magnitude and dip direction of the basement  
739 fabrics are strongly correlated with those of the faults (see stereographic contours and poles  
740 to fault planes in Figures 9bi and 9ciii).

741

#### 742 4.3.2 *Txizita Horst*

743 In the absence of high-resolution aeromagnetic data over the Txizita Horst, we map  
744 basement fabrics in both the low-resolution SADC aeromagnetic grid (Figures 4b, 5a) and  
745 the topographic relief map (red lines in Figure 9a). The frequency-azimuth distributions of  
746 the metamorphic fabric lineaments in both datasets (Figure 9di-ii) show a multimodal  
747 distribution with consistent dominant sets trending ENE to NE ( $\sim 079^\circ$  from aeromagnetics,  
748  $\sim 069^\circ$  from topographic relief) and NW-SE ( $\sim 132^\circ$  from aeromagnetics,  $145^\circ$  from  
749 topographic relief). The plots also show a minor N to NNE set ( $\sim 011^\circ$  from aeromagnetics,

750  
751  
752  
753  
754  
755  
756  
757  
758  
759  
760  
761  
762  
763  
764  
765  
766  
767  
768  
769  
770  
771  
772  
773  
774  
775  
776  
777  
778  
779

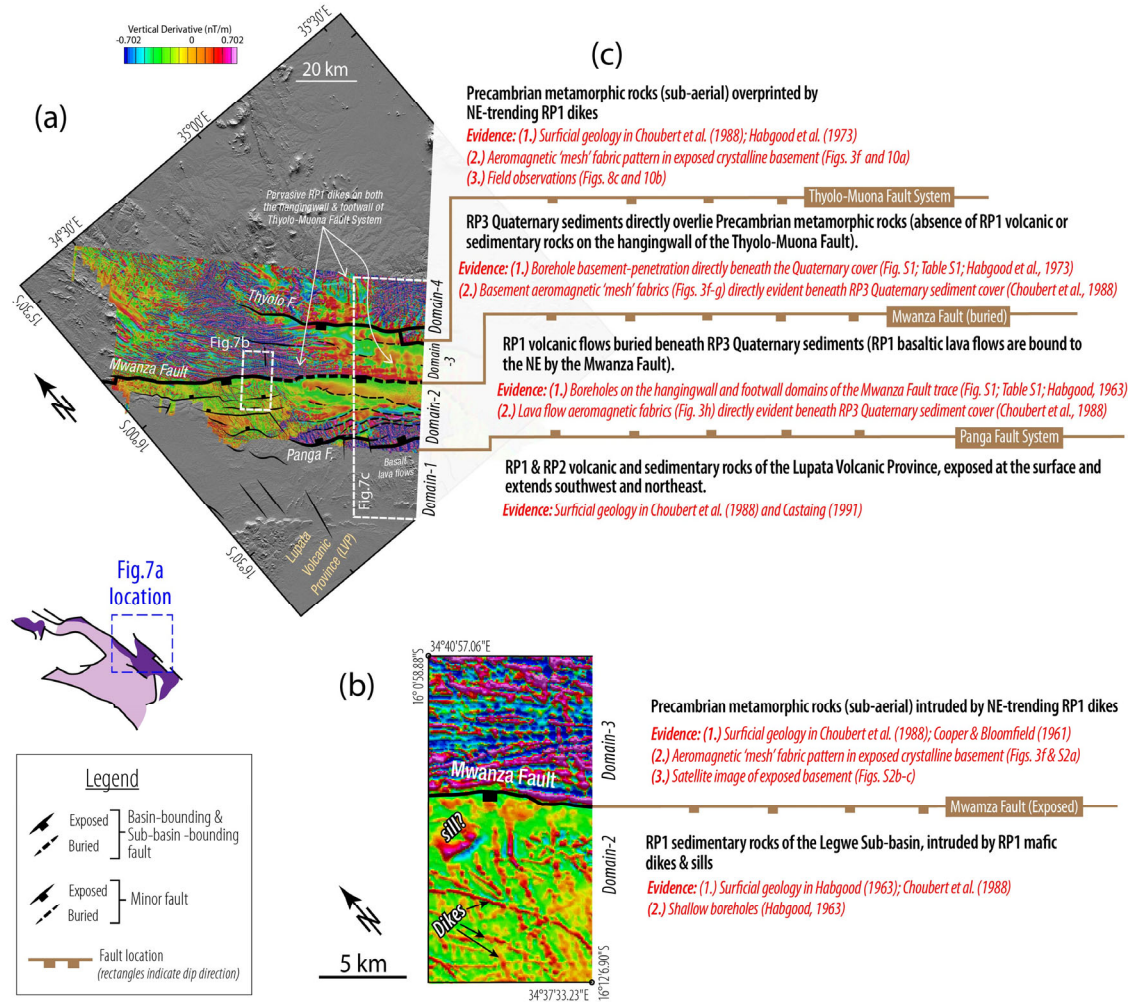
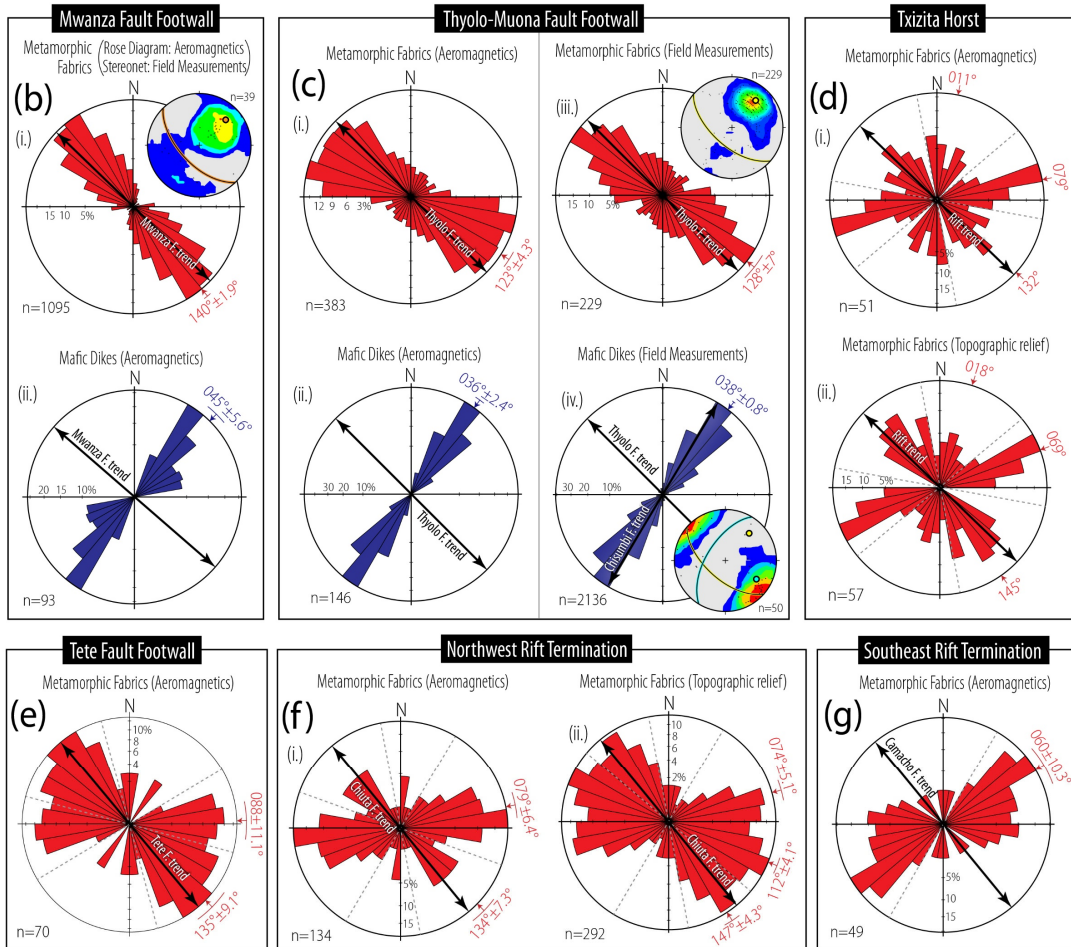
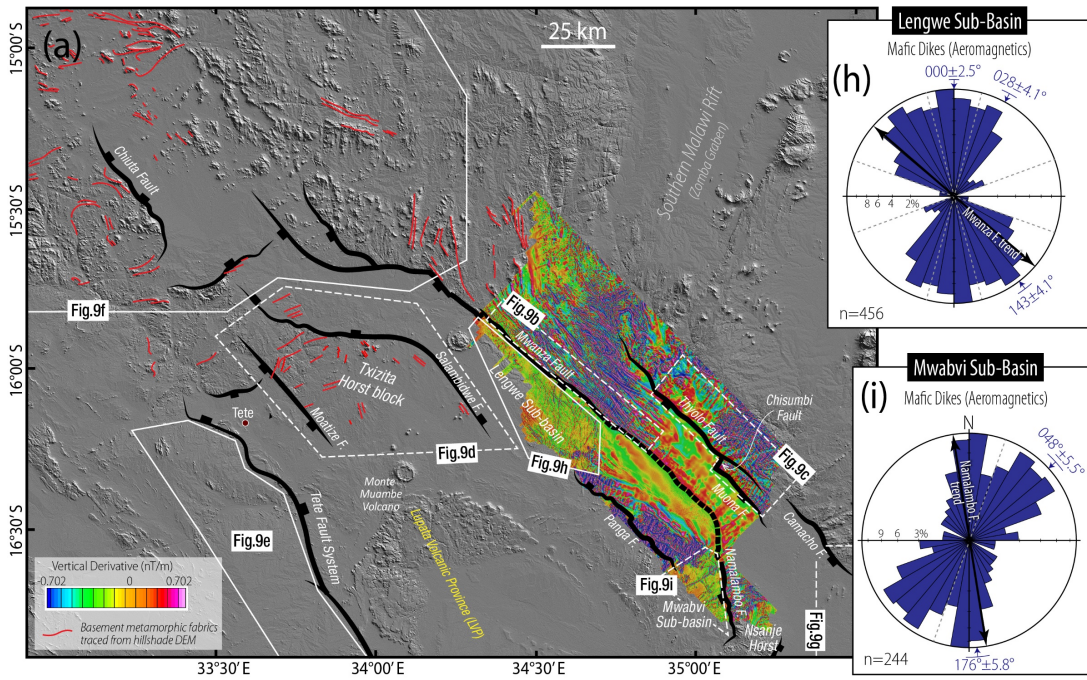


**Figure 7. Borehole and magnetic fabric constraints on the relative timing of strain localization in the Lower Shire sub-basin.** (a) Map covering parts of the Lengwe and Lower Shire sub-basins (same map in Figure 3c). (b) Zoomed-in map of the eastern portion of the Lengwe Sub-basin (see location in inset sketch map). The interpretations of the distinct magnetic domains (bold black texts in Figures 7b and 7c) are constrained by multiple independent datasets and observations (italicized red texts). In Figures 7b and 7c, the referenced borehole locations and associated data are provided in Supplementary Figures S3a-b and Supplementary Table S1.

780  
781  
782  
783  
784  
785  
786  
787  
788  
789  
790  
791  
792  
793  
794  
795  
796  
797  
798  
799  
800  
801  
802  
803  
804  
805  
806



807

808 **Figure 9. Structural trends of inherited basement fabrics (foliation) and syn-rift igneous dikes.** (a)  
 809 Shuttle Radar Topography Mission (SRTM) DEM hillshade map of the Shire Rift Zone overlaid with vertical  
 810 derivative aeromagnetic map of the Malawi part of the rift. The red lines represent topographic expressions of  
 811 basement fabrics around the rift (providing independent information on pre-rift basement fabrics, see Figs. 9d  
 812 & 9f); (b - c) Azimuth-frequency distribution of basement metamorphic fabrics and mafic dikes along the  
 813 footwall of (b) the Mwanza Fault, and (c) the Thyolo-Muona Fault System; (d - g) Frequency-azimuth  
 814 distribution of metamorphic fabrics within the Txizita Horst block (9d), footwall of the Tete Fault System (9e),  
 815 and the northwestern (9f) and southeastern (9g) rift terminations zones; (g - h) Frequency-azimuth  
 816 distribution of mafic igneous dikes in the Lengwe (9h) and Mwabvi sub-basins (9i). Insets of stereographic  
 817 projections (equal-area) represent poles to planes with 2 interval Kamb contours, and great circles with  
 818 colored halos represent the Mwanza Fault plane ( $136^{\circ}/60^{\circ}$  in 9bi), Thyolo Fault plane ( $131^{\circ}/60^{\circ}$  in 9ciii-iv),  
 819 and Chisumbi Fault ( $211^{\circ}/60^{\circ}$  in 9civ). The  $60^{\circ}$  dip of fault planes is obtained from previous field observation  
 820 along the Thyolo Fault (Wedmore et al., 2020). In Fig. 9ciii, the rose and stereographic projection both consist  
 821 of a combination of field measurements collected during our field visit ( $n=38$ ) and those previously collected  
 822 by the Malawi Geological Survey ( $n=191$ ; Habgood et al., 1973). Whereas, in Fig. 9civ, although the rose plot  
 823 includes a combination of our field measurements ( $n=50$ ) and those in Habgood et al. (1973) ( $n=2086$ ), the  
 824 stereographic projection consists only of our field measurements as the dip of dikes were not reported in  
 825 Habgood et al. (1973). Black dashed lines in rose plots represent frequency minima used for modal set grouping  
 826 and calculation of circular vector mean for the modal sets.

827

828

829  $\sim 018^{\circ}$  from topographic relief). The NE-trending fabrics appear to dominate most of the  
 830 horst, whereas the NW-trending, which set is parallel to the rift trend, is primarily localized  
 831 at the center and along the northeastern margin of the horst in the footwall of the  
 832 Salambidwe Fault (Figures 4b, 5a, 9a).

833

#### 834 4.3.3 *The Tete Border Fault and Environs*

835 Since the basement fabrics are poorly expressed in the topographic relief map (Figure  
 836 9a), we only obtain measurements of basement fabrics from the regional aeromagnetic grid  
 837 (Figures 4b, 5a). The result shows a very prominent NW-SE trend ( $\sim 135^{\circ}$ ) which is sub-  
 838 parallel to the trend of the Tete Fault system (Figure 9e). However, we also observe a  
 839 secondary set in the data which trends E-W ( $\sim 088^{\circ}$ ) and is collocated with a kink in the trend  
 840 of Tete Fault's trace (Figure 5a).

841

#### 842 4.3.4 *The Rift Termination Zones*

843 At regional-scale, within the northwestern rift termination zone (i.e., vicinity of the  
 844 Chiuta Sub-basin), the available aeromagnetic grid shows that the basement fabrics are

845 characterized by multimodal trends (Figure 9fi-ii) in which an ENE trend ( $\sim 079^\circ$  from  
846 aeromagnetics,  $\sim 074^\circ$  from topographic relief) and NW-SE ( $134^\circ$  from aeromagnetics,  
847  $\sim 147^\circ$  from topographic relief) trend are most prominent. The NW-SE fabric set is parallel  
848 to the trend of the Chiuta Fault ( $\sim 137^\circ$ ). Whereas at the southeastern rift termination zone  
849 (SE tip of the Camacho Fault; Figure 9a), the basement is dominated by NE-SW -trending  
850 fabrics with a mean trend of  $\sim 060^\circ$  (Figure 9g), which are sub-orthogonal to the Camacho  
851 Fault trend ( $\sim 140^\circ$ ).

852

#### 853 **4.4 Syn-Rift Magmatic Structures in the Shire Rift Zone**

854 Observations during our field visit (e.g., Figure 3b) and a compiled surficial geologic  
855 map of the SRZ (Figure 2) raise the need to explore the patterns and distribution of syn-rift  
856 diking and ring-shaped igneous structures that dominate the rift zone. The aeromagnetic  
857 fabric patterns and lineament 'types' observable in the filtered aeromagnetic grids include:  
858 1) Broad clusters of parallel, elongate high-frequency, high-amplitude short-wavelength  
859 magnetic fabrics in exposed basement (Figure 4d), representing sub-vertical basement  
860 metamorphic foliation observable in field outcrops (Figures 3b-c); 2) Discrete cross-cutting  
861 lineaments of high-amplitude short-wavelength character enclosed by longer-wavelength  
862 magnetic-low anomalies, representing mafic igneous dike intrusions within sedimentary  
863 sequences in Lengwe and Mwabvi Sub-basins (e.g., Figure 4e) observable in exhumed  
864 Mesozoic syn-rift outcrops and boreholes (Habgood, 1963), among which lineament sets  
865 show different amplitudes indicative of different emplacement depths, here in described as  
866 "strong discrete lineaments, 'SDL'" (shallower dikes?) and "weak discrete lineaments,  
867 'WDL'" (deep-seated dikes?); 3) Broad zones of high-amplitude mesh pattern fabrics in  
868 exposed basement (Figure 4f), representing metamorphic foliation overprinted by cross-  
869 cutting mafic dikes observable in field exposures (Figures S4a-c); 4) Broad zones of low-  
870 amplitude mesh pattern fabrics in intra-basinal areas of Quaternary-age sedimentary cover  
871 (Figure 4g), occurring as the buried lateral continuation of the metamorphic basement  
872 hosting cross-cutting mafic dikes (i.e. fabric type #3 buried beneath unconsolidated alluvial  
873 sediments); and 5) Broad zones of compact linear bands of chaotic high-amplitude high-

874 frequency magnetic fabrics (Figure 4h) collocated with exposed or shallowly buried  
875 Mesozoic basaltic flows in the Mwabvi Sub-Basin (Figure 2; Habgood, 1963).

876 The basalt-related magnetic fabrics are cut and truncated by a system of sub-parallel  
877 rectilinear abrupt gradients that correspond to faults (e.g., Panga Fault, observable in the  
878 field and in topographic relief map; Figures 2, 4c). Also, the amplitude of the basalt-related  
879 magnetic anomalies decreases northeastward towards the Mwanza Fault as the depth of  
880 burial of the volcanic flows increases. Overall, in eastern SRZ in Malawi where high-  
881 resolution aeromagnetic data is available (Figures 4a and 4c), we mapped and analyzed the  
882 dike-related magnetic lineaments. In other parts of the rift zone where lower-resolution  
883 aeromagnetic data is the only available subsurface data (Figures 4a and 4b), we show the  
884 presence and distribution of prominent ring-shaped magnetic anomalies and describe their  
885 associations with surface igneous complexes in the rift.

886

#### 887 4.4.1 *Lengwe and Mwabvi Sub-Basins*

888 The high-resolution aeromagnetic data reveal the presence of a more complex  
889 network of cross-cutting dike-related magnetic lineaments in the Lengwe Sub-basin than in  
890 the Mwabvi Sub-basin (Figures S5a-b). The frequency-azimuth distribution of the Lengwe  
891 dikes (Figure 9h) is multimodal with three dominant sets trending N-S ( $\sim 000^\circ$ ), NNE-SSW  
892 ( $\sim 028^\circ$ ), and NW-SE ( $\sim 143^\circ$ ). The NW-SE dike segments are generally sub-parallel to the  
893 intrabasin faults, the Mwanza border fault, and the overall rift trend (Figure S5).

894 In the southern section of the Mwabvi Sub-basin where the dikes are observable, the data  
895 (Figure 8i) shows only two dominant sets which include a N-S ( $\sim 176^\circ$ ) and NE-SW ( $\sim 048^\circ$ )  
896 trend. The N-S trending dike segments are parallel to the strike of the Namalambo Fault  
897 representing the border fault in that part of the basin (Figure S5b). Whereas the NE-trending  
898 dikes, some of which extend across the border fault, are parallel to the trend of the basement  
899 fabrics in the Namalambi Fault footwall (LSZ and surrounding fabrics at the SE rift  
900 termination zone; Figure 5a). Further, some of the NE dikes that extend across the  
901 Namalambo Fault are collocated with the zone of burial of the northern tip of the Namalambo  
902 Fault, and en-echelon transverse offsets of the fault beneath the Quaternary cover ("T" in  
903 Figure S5b).

904 4.4.2 Mwanza and Thyolo-Muona Border Fault Footwalls

905 In the footwall of the Mwanza Fault, the dikes show a dominant (unimodal) NE-SW  
 906 trend,  $\sim 045^\circ$  (Figures 9bii, S4a-c). Similarly, on both the footwalls and hanging walls of the  
 907 Thyolo-Muona Fault system, the dikes show a prominent unimodal trend of  $\sim 036^\circ$  (Figures  
 908 9cii, 10a-b), consistent with field measurements in their footwalls ( $\sim 038^\circ$ ; Figure 9civ and  
 909 stereographic projection). Our field measurements (stereographic contours in Figure 9civ)  
 910 show that in dip view, the dikes occur in a conjugate set with some dipping to the NW and  
 911 others to the NE. Although the Thyolo and Muona Faults are sub-orthogonal to the dikes, the  
 912 Chisumbi Fault ( $\sim 031^\circ$ ) strikes parallel to the dikes and shows strong alignment in dip  
 913 magnitude and direction with the NW-dipping dike set (see pole to Chisumbi Fault plane in  
 914 Figure 9civ).

915

916

917

918

919

920

921

922

923

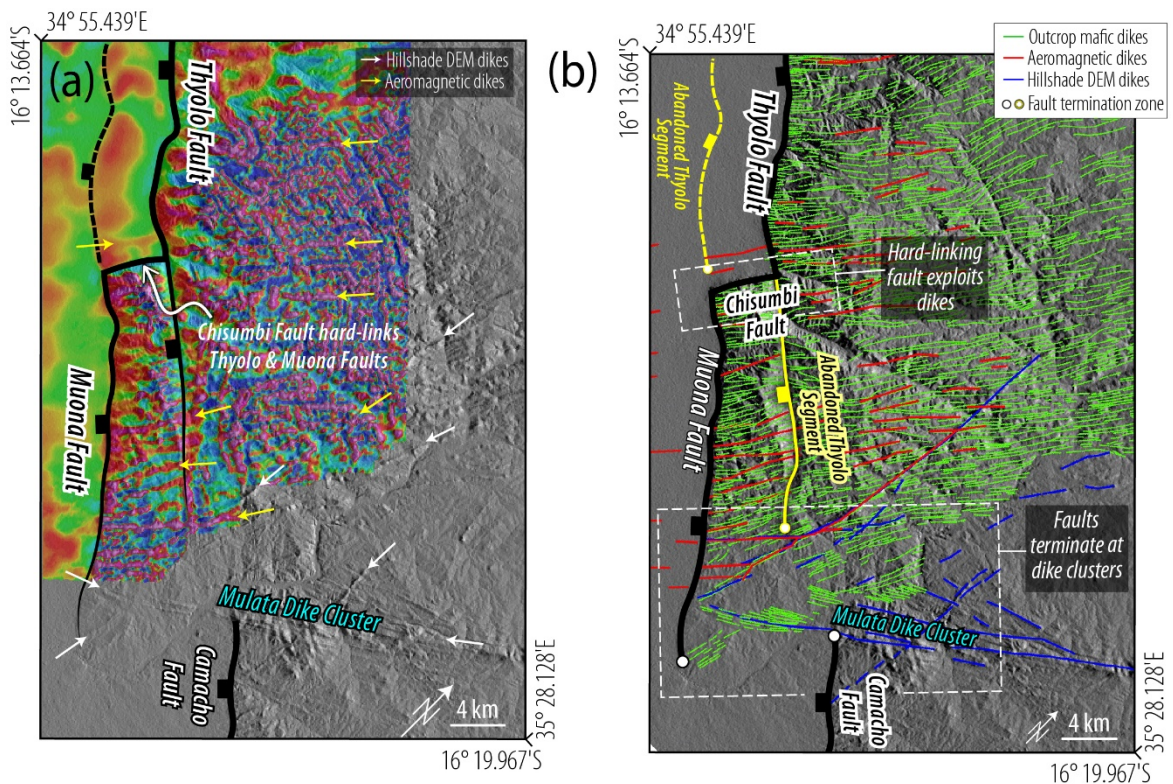
924

925

926

927

928



929 **Figure 10. Relationships between the rift border faults and the early phase (RP1-RP2) mafic dikes.** (a)  
 930 Filtered aeromagnetic map (location: SE half of polygon "Fig. 9c" in Figure 9a) showing aeromagnetic dike  
 931 lineaments (yellow arrows) and topographic expression of dikes (white arrows); (b) Map of same area in Figure  
 932 10a, showing the interpreted mafic dike aeromagnetic lineaments (red lines), SRTM hillshade dike lineaments  
 933 (blue lines), and those from published field mapping (green lines; Habgood et al., 1963).

#### 934 4.4.3 *Lupata Volcanic Province (LVP)*

935 The regional aeromagnetic grid shows that both the Monte Muambe Volcano (MV)  
936 and Salambidwe Igneous Structure (SIS) are characterized by prominent ~10 km-wide ring-  
937 shaped magnetic-high anomalies (Figure 4b). South of the Monte Muambe Volcano, we  
938 identify several similarly-sized ring-shaped high-amplitude magnetic anomalies (with 7.5 –  
939 19 km diameters) distributed over a distance of 140 km (Figures 4b and 5a). These ring-  
940 shaped anomalies do not correspond to any distinct surface topographic feature. However,  
941 the anomalies delineate a NW-trending belt along the rift axis.

942

## 943 5 DISCUSSION

### 944 5.1 New Interpretation of the SRZ Architecture

945 Although the broad geologic history of the SRZ has been previously identified  
946 (Castaing, 1991), only the Lengwe, Mwabvi, and Lower Shire depocenters were  
947 distinguished while the rest of the basin was referred to as the Middle Zambezi Valley  
948 (Castaing, 1991, Chisenga et al., 2019). Thus, the detailed structure, rift basin  
949 compartmentalization, and the associations with the phases of extension are not known. The  
950 extent and distribution of fault-bounded Mesozoic and Cenozoic sedimentary and  
951 volcanoclastic deposits in the Shire Rift (Figure 2) represent a multiphase rift zone with  
952 compartmentalization (Figure 5b) that is facilitated by complex brittle and magmatic  
953 deformation (Figure 8). Based on the integration of surficial geology (Figure 2) and  
954 structural interpretations from filtered aeromagnetic datasets, we identified seven  
955 structural domains within the basin, which include the Lower Shire, Mwabvi, Lengwe, Monte  
956 Muambe, Moatize, Chiuta, and Lupata Sub-Basins (Figure 5b).

957 Based on the presence of basement-sedimentary magmatic intrusions, volcanic  
958 deposits, and timing of magmatic activities in the SRZ, we characterized the sub-basins into  
959 magmatic and non-magmatic categories. Considering that the Lupata Sub-Basin houses the  
960 Lupata Volcanic Province (LVP) where multi-phase rejuvenation of widespread intra-rift  
961 volcanism localized during RP1-RP2, we suggest that this sub-basin likely hosts some of the  
962 richest information on multiphase early-stage magmatic rifting, yet it remains poorly  
963 understood. Also, the spatial extents of syn-rift sequences across the SRZ (Figures 2) suggest

964 that the Lengwe, Mwabvi, Moatize, and Monte Muanbe Sub-basins were established and  
965 most active during RP1 (Figure 11a). Late-RP1 magmatic plumbing of the rift appears to be  
966 basin-scale (Castaing, 1991). However, RP2 tectonic activities largely involved the focusing  
967 of intra-rift volcanism in the LVP, the Salambidwe area of the Lengwe Sub-basin, and  
968 localization of off-rift magmatism outboard of the evolving rift (Chilwa Alkaline Province,  
969 CAP; Figures 2, 8, 11b).

970

### 971 *5.1.1 Possible Cenozoic Establishment of the Lower-Shire and Chiuta Sub-Basins*

972 As is the case in many onshore basins in East Africa, the lack of surface-to-basement  
973 wells limits the understanding of the spatiotemporal rift propagation at the segment scale. A  
974 similar challenge arises here in the SRZ, where available legacy boreholes only sampled  
975 shallow depths in the Chiuta and Lower Shire Sub-basins. However, based on the most up-  
976 to-date compilation of surface and subsurface data on the SRZ, we infer the most probable  
977 rift history of the two sub-basins with the most widespread accumulations of RP3 deposits.

978 Bloomfield (1958), Cooper and Bloomfield (1961), and Habgood (1963) documented  
979 the presence of ~1.2 km-wide hydrothermal alteration zone along the escarpment and  
980 footwalls of the Mwanza Fault and Namalambo Fault. The alteration zones are characterized  
981 by unbroken silicic and calcite hydrothermal veins with associated epidote and pyrite  
982 mineralization, and they preserve evidence of multiple episodes of fluid alteration  
983 (Bloomfield, 1958). Along the Namalambo Fault zone, the veins crosscut both the  
984 Precambrian basement and brecciated RP1 diabase intrusions (Bloomfield, 1958). Based on  
985 the observed cross-cutting relationship and the large-scale 'unbroken' structure of the veins,  
986 this pervasive hydrothermal event has been interpreted to have occurred during the Late  
987 Cretaceous rifting activity (RP2). However, field observations along the Thyolo-Muona Fault  
988 zones show no evidence of fluid alteration (this study, and others: Williams et al., 2019;  
989 Wedmore et al., 2020), suggesting that the fault zones did not undergo the same  
990 hydrothermal events observed along the Mwanza and Namalambo Faults. These  
991 observations suggest that the Thyolo-Muona Fault System was likely not established until  
992 the RP3.

993           The absence of Mesozoic volcanic rocks in the hanging wall of the Thyolo-Muona  
994 border fault suggests that the Lower Shire Sub-basin was most likely not established as a  
995 major depocenter during the magmatic RP1-2 rift phases (Figures 7a-c, 11c). Also, in the  
996 other on-shore Eastern Africa rift basins that accommodated RP1-RP2 rifting and have been  
997 reactivated in the Cenozoic, outcrops of the Mesozoic syn-rift units have been documented  
998 along their uplifted flexural margins (e.g., Rukwa Rift, Luangwa Rift, Northern Malawi Rift;  
999 Bennett, 1989; Ring 1995; Delvaux, 2001; Kolawole et al., 2018; Daly et al., 2020). However,  
1000 in the uplifted flexural margins of the Chiuta Sub-basin and hanging walls of the Thyolo-  
1001 Muona Fault, outcrops of RP1-RP2 sedimentary rocks are absent. Also, the magnetic anomaly  
1002 pattern in the hanging walls of the Thyolo and Muona Faults (see Figure 7a) primarily  
1003 exhibits long-wavelength anomalies of buried metamorphic fabrics crosscut by mafic dikes,  
1004 both confined to the crystalline basement beneath the sedimentary cover (Figures 4f-g).  
1005 Whereas, in the hanging wall of the Mwanza and Namalambo faults where RP1-RP2 syn-rift  
1006 sequences are widespread, the magnetic fabric pattern is dominated by discrete magnetic-  
1007 high short-wavelength lineament anomalies of mafic dikes that intruded the syn-rift  
1008 sedimentary sequences (Figures 4e, S5a-b; also see field and borehole observations in  
1009 Habgood, 1963; Castaing et al., 1991). In essence, the Thyolo-Muona fault hanging wall lacks  
1010 the presence of sedimentary sequences with intruded mafic dikes.

1011           The modeled depth-to-crystalline-basement in the Chiuta Sub-basin and Thyolo-  
1012 Muona Fault hanging wall (Figures 6a-b) generally shows <1.5 km depth, which is consistent  
1013 with basement depths in the nearby southern Malawi Rift (maximum of 1.6 km) where an  
1014 absence of Mesozoic rifting has been similarly inferred (Scholz et al., 2020; Williams et al.,  
1015 2021). At regional scales, geodetic stretching rates generally decrease towards the euler pole  
1016 of plate rotation, such that within a sub-region of contemporary rifting such as the Shire Rift  
1017 Zone and Southern Malawi Rift, crustal stretching rates can be assumed to be relatively  
1018 uniform spatially (~2.2 mm/yr; Stamps et al., 2018; Wedmore et al., 2021). Thus, if both the  
1019 southern Malawi Rift and Lower Shire Graben have experienced tectonic extension for the  
1020 same length of time, the maximum throws on the active border faults should be relatively  
1021 similar, assuming a uniform time-averaged crustal stretching rates across the sub-region.  
1022 Therefore, the similarity of maximum border fault throws in southern Malawi Rift to those

1023 of the Chiuta Sub-Basin and Thyolo-Muona Fault hanging wall, given by maximum depth-to-  
1024 basement along the border faults, suggests that the three areas are likely coeval.

1025 Dixey (1925) also noted the absence of RP1 and RP2 syn-rift sediments in the Lower  
1026 Shire Sub-basin (i.e., in the area between Mwanza Fault and Thyolo-Muona Fault) and  
1027 speculated on ~400 m Jurassic-age uplift event (immediately after RP1) and additional ~1.2  
1028 km Late Miocene-age localized uplift event (after RP2) within the sub-basin that could have  
1029 led to the erosion of both the RP1 and RP2 syn-rift deposits immediately after each rift phase.  
1030 These speculations are problematic considering that 1) the suggested magnitude of post RP1  
1031 uplift implies that the Lower Shire area (i.e., Mwanza Fault's footwall) did not experience  
1032 significant tectonic subsidence during RP1, and 2) results from thermochronology studies in  
1033 the area does not support the occurrence of a localized uplift, but rather a regional-scale  
1034 Paleogene tectonic uplift (Daszinnies et al., 2008; Ojo et al., 2020 *in review*). The studies show  
1035 the occurrence of regional Eocene-age uplift associated with the initiation of East African Rift  
1036 System (Daszinnies et al., 2008) and Late Cenozoic footwall uplift along the Thyolo Fault (i.e.,  
1037 RP3 rift border faulting; Ojo et al., 2020 *in review*).

1038 Coal deposits are known to preserve excellent records of maximum  
1039 paleotemperatures that they have been exposed to (e.g., Hunt et al., 2002; Singh et al., 2007).  
1040 Geochemical analyses of the Karoo-age (RP1) coal seams of the Lengwe-Mwabvi Sub-basins  
1041 show approximate carbon content of 75.7 % and volatile matter of ~25 % on a dry ash free  
1042 basis (Habgood, 1963). These values indicate orthobituminous coals of high to medium  
1043 volatile bituminous rank, corresponding to vitrinite reflectance of ~0.9 - 1.5 % (Hunt et al.,  
1044 2002; Suárez-Ruiz & Crelling, 2008). Assuming an average geothermal gradient (25-30  
1045 °C/km in continental crust) and normal burial-and-exhumation paths, these RP1 coal-rich  
1046 units would have been buried to about ~3 - 4 km depths to attain the estimated thermal  
1047 maturity level (Bjørlykke, 1989) prior to exhumation. However, such a simple burial-and-  
1048 exhumation history cannot be assumed here considering the RP1 and RP2 magmatic events  
1049 and associated intrusions into the coal-rich syn-rift sequences (Habgood, 1963; Figs. S5a-b)  
1050 and the strong thermal maturation effects of such extraneous heat sources on coal deposits  
1051 (e.g., Stewart et al., 2005; Singh et al., 2007). Therefore, we infer that the exhumed RP1 units

1052 in the Lengwe-Mwabvi Sub-basins (adjacent to the Lower Shire Sub-basin) were likely only  
1053 buried to depths much shallower than 4 km prior to their Cenozoic exhumation.

1054 We acknowledge that it is still possible that the current locations of the Chiuta Sub-  
1055 basin and Thyolo-Muona Fault's hanging wall area hosted syn-rift Mesozoic depocenters that  
1056 were eroded off at sometime between the Cretaceous and Cenozoic rift phase. However, such  
1057 depocenters may have been significantly smaller and shallower (diffused rifting?) than those  
1058 hosted and preserved in the other sub-basins with widespread outcrops of RP1-2 deposits:  
1059 Lengwe, Mwabvi, Moatize, Monte-Muambe, and Lupata Sub-basins. Therefore, we argue that  
1060 that the Chiuta Fault and the Thyolo-Muona Fault Systems were likely not established as  
1061 major syn-rift depocenters along the SRZ until the RP3. Thus, it is still possible that isolated  
1062 pockets of small RP1-RP2 sedimentary deposits may be preserved at the deepest parts of  
1063 these major RP3 sub-basins, but would require a future basement-penetrating drilling  
1064 campaign to confirm. Also, we emphasize that unlike the RP1-RP2 strain accommodation in  
1065 the SRZ that recorded pronounced magma-assisted rifting, the RP3 strain accommodation in  
1066 the rift zone is not magma-assisted.

1067

## 1068 **5.2 Pulsed Rift Propagation in the SRZ: Multiphase Strain Migration and Sub-Basin** 1069 **Abandonment**

1070 The absence of major RP1-RP2 depocenters in the Chiuta Sub-basin and Thyolo-  
1071 Muona Fault's hanging wall suggests that the RP1-RP2 rift deformation and subsidence were  
1072 largely confined to the region bounded by the Mwanza-Namalambo Fault to the northeast  
1073 and the Tete Fault to the southwest. To the northwest, the RP1-RP2 rift bifurcates and  
1074 appears to have terminated at or near the intersection of the rift with the Senangoe Shear  
1075 Zone. To the southeast, the rift-bounding Namalambo Fault also terminates at the Lurio  
1076 Shear Zone. However, the localization of the Chiuta Sub-basin to the northwest of the  
1077 Sanangoe Shear Zone in RP3 suggests that the Cenozoic rifting in the SRZ recorded a  
1078 resurgence of lateral along-trend propagation of the rift basin. The absence of RP3 tectonic  
1079 activity in the LVP and surrounding sub-basins suggests that this previously active magmatic  
1080 domain of the rift was largely abandoned after RP2, and strain has migrated further

1081 northwest and east/northeast of the basin. The RP3 rift-orthogonal strain migration into the  
1082 margin of the older basin led to the development of the Lower Shire Graben.

1083         This sequence of temporal rift evolution describes a pulsed pattern of lateral rift  
1084 propagation in which continuous lateral propagation of the tip of an active rift is stalled for  
1085 a considerable period, after which rift lengthening resumes (Courtilot 1982; Van Wijk and  
1086 Blackman, 2005). However, questions arise as to the forcing mechanism behind the large-  
1087 scale abandonment of the RP1-RP2 basin and rift-orthogonal strain migration into the  
1088 northeastern rift margin. Strain migration during multiphase rifting is not uncommon in the  
1089 tectonic records of rifted continental margins and failed continental rifts (e.g., Braun, 1992;  
1090 Bell et al., 2014; Fazlikhani et al., 2020). In the SRZ, the Mesozoic phases of rifting were  
1091 accompanied by voluminous basaltic magmatism (Figures 2 and 11; Castaing et al, 1991),  
1092 and gravity modelling reveal the possible presence of sub-crustal intrusive bodies beneath  
1093 the SRZ-related RP2 igneous provinces (Njunju et al., 2019b).

1094         Therefore, an explanation for the basin abandonment and strain migration could be  
1095 a possible strengthening (healing) of the crust and lithospheric mantle beneath the early-  
1096 phase sub-basins, facilitated by a prolonged inter-rift period between RP2 and RP3 after the  
1097 RP1-RP2 magma-assisted crustal thinning. This inference is supported by lithospheric-scale  
1098 rift models (e.g., Braun, 1992; Naliboff and Buitter, 2015). Braun (1992) argued that the  
1099 absence of RP3 reactivation in the RP1-RP2 rift basins flanking the northern Malawi Rift  
1100 (Ruhuhu and Maniamba Rifts; Figure 1a) is due to inter-rift lithospheric healing, such that  
1101 relatively unstretched regions of the mobile belts served as strain concentrators in the RP3.  
1102 The integrated crustal strength of the magmatic RP1-RP2 rift zone may likely have surpassed  
1103 that of the surrounding areas (Naliboff and Buitter, 2015), such that the initiation of Cenozoic  
1104 crustal stretching (RP3) favored the migration of strain into the surrounding areas. We note  
1105 that although other magmatic RP1-2 rifts in the region such as the Zambezi Rift also show a  
1106 similar style of large-scale post-RP2 abandonment, the border faults of the Luangwa Rift are  
1107 experiencing RP3 reactivation (Daly et al., 2020). However, it is also not yet clear if inter-  
1108 RP2-3 lithospheric healing also controlled the absence of resurgent magmatic rifting in the  
1109 RP3 along the SRZ, considering that the basin was largely magmatic in the previous phases  
1110 of extension.

1111

### 1112 **5.3 Inheritance of Weakening Structures: Strain Localization Through the** 1113 **Exploitation of Intra-Basement Weak Zones**

#### 1114 *5.3.1 Early-Phase (RP1) Border Faulting*

1115 If the Mwanza-Namalambo and Tete Faults are the main Mesozoic border faults of the  
1116 SRZ, based on the present-day surface locations of the faults and exposures of syn-rift basin-  
1117 fill, we estimate that the RP1 basin is a NW-trending rift basin that bifurcates  
1118 northwestwards into two 20-25 km-wide branches, covering a total of ~17,299 km<sup>2</sup> areal  
1119 extent over a length of ~200 km (Figures 5b, 11a). The branches are also confined by ‘inner’  
1120 border faults, Moatize, and Salambidwe Faults, which juxtapose the rift-fill against the pre-  
1121 rift basement of the Txizita Horst (Figure 5d).

1122 Along the eastern rift shoulder, the Mwanza Fault’s strike and dip show strong  
1123 alignment with those of the underlying pre-rift basement metamorphic fabrics (Figures 9b,  
1124 11a). In the northern Lengwe Sub-basin where the Mwanza Fault rotates counter-clockwise,  
1125 field observations in Barr and Brown (1987) show that the fault is collocated with- and  
1126 follows the easternmost segment of the crustal-scale Precambrian Sanangoe Shear Zone  
1127 (SSZ). Likewise, the Salambidwe Fault is parallel to the trends of the basement fabrics  
1128 (Figures 4a, 9a). However, to the SE, the N-trending Namalambo border fault cuts across the  
1129 NE-trending basement fabrics of the Lurio Shear Zone (LSZ), except for its southernmost tip  
1130 which rotates clockwise and follows the trend of the basement fabrics (Figure 5a; Bloomfield,  
1131 1958). We note that the southernmost part of the Namalambo Fault bends into a NE trend  
1132 which parallels the LSZ (Figures 4b, 5a). Along the western rift shoulder, the northernmost  
1133 sections of the Tete Fault trend parallel to aeromagnetic basement fabrics (Figures 4b and  
1134 9e), which is consistent with observations in published geologic maps (Choubert et al.,  
1135 1988). Whereas, the Moatize Fault, the inner border fault of the Moatize rift branch, appears  
1136 to crosscut the metamorphic basement fabrics (Figures 4b, 5a, 9a). Overall, based on these  
1137 observations, we suggest that that the RP1 eastern border fault (Mwanza Fault) exploited  
1138 the pre-rift basement fabrics along most of its length, whereas the western border fault (Tete  
1139 Fault) partially exploited the basement fabrics.

1140

1141  
1142  
1143  
1144  
1145  
1146  
1147  
1148  
1149  
1150  
1151  
1152  
1153  
1154  
1155  
1156  
1157  
1158  
1159  
1160  
1161  
1162  
1163  
1164  
1165  
1166  
1167  
1168  
1169  
1170

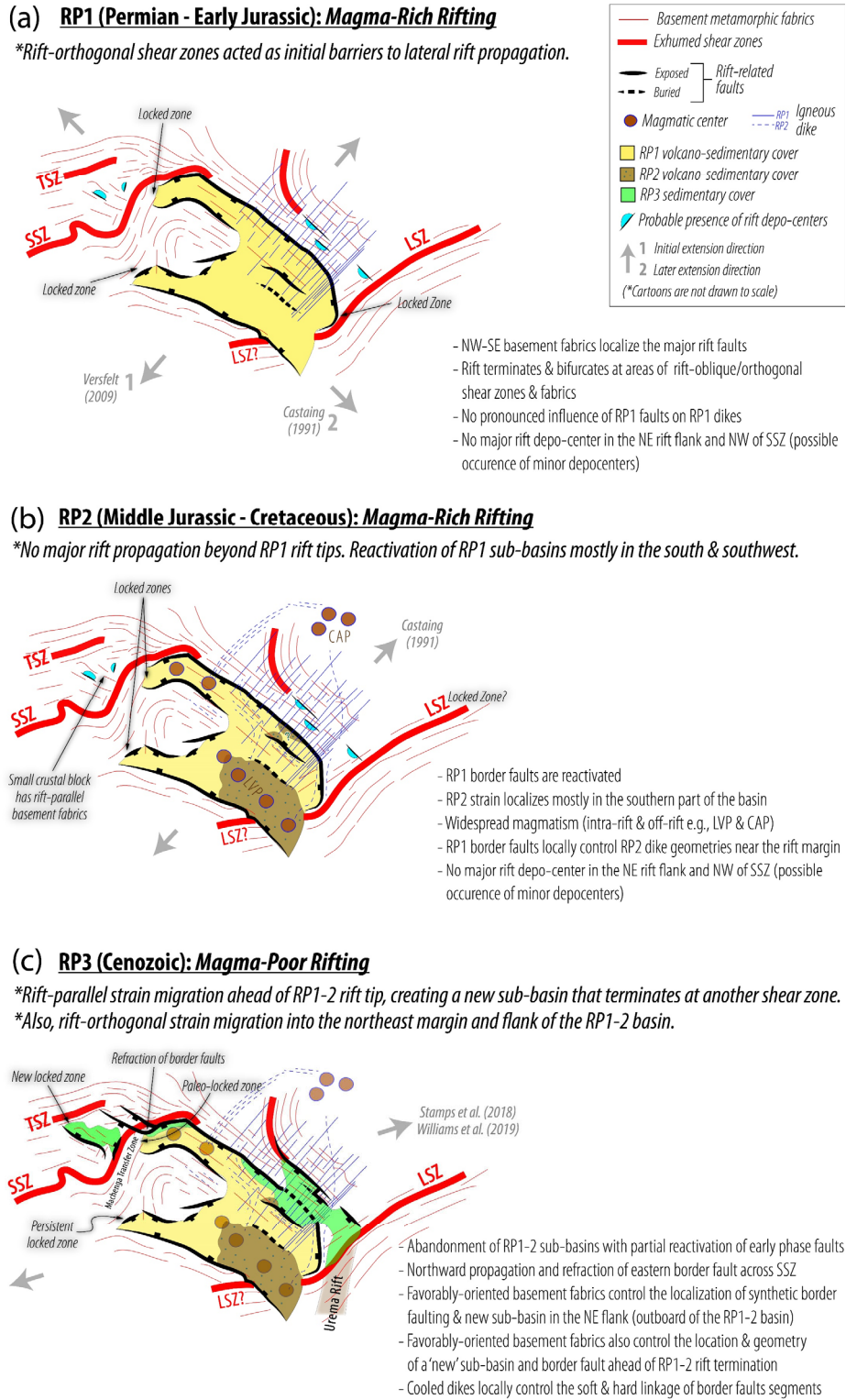


**Figure 11.** Cartoons summarizing the multiphase evolution and strain migration in the Shire Rift Zone, based on observations in this study. LSZ: Lurio Shear Zone, MDC: Mulata Dike Cluster, SSZ: Sanangoè Shear Zone.

1171           The large-scale alignment of the early-phase border faults with those of the  
1172 underlying pre-rift basement metamorphic fabrics suggests that the border fault likely  
1173 exploited the basement fabrics during rift initiation. Due to limited field access, we are only  
1174 able to assess the 3-D component of the alignment in the Malawi extension of the SRZ.  
1175 However, our observations along the Mwanza Fault escarpment show a correspondence  
1176 between the strike, dip magnitude, and dip direction of the basement fabrics with those of  
1177 the border fault. The gneissic basement foliation along the SRZ border faults constitute  
1178 planes of mechanical weakness that was exploited by brittle deformation during the early-  
1179 rift extension (e.g., Donath, 1961; Youash, 1969; Ranalli and Yin, 1990; Morley, 1999, 2010).  
1180 However, the inferred NW-SE regional extension direction for RP1 (Castaing, 1991) is not  
1181 compatible with the development of NW-trending faults, and even less likely in a crust with  
1182 NW-trending pre-rift mechanical anisotropy (Youash, 1969; Morley, 1999). Although  
1183 Castaing (1991) inferred strike-slip kinematics for the RP1 rifting, the rift structure lacks the  
1184 map-view rhombic geometry or associated Reidel pattern faulting that is typical of strike-  
1185 slip and transtensional basins.

1186           Thus, we argue that it is more likely that the SRZ first accommodated a NE-oriented  
1187 tectonic extension during early RP1, and in late RP1, the rotation of extension direction into  
1188 a NW-SE direction facilitated an oblique-normal or strike-slip reactivation of the early rift  
1189 border faults (Figure 11a). This is supported by the Lower Jurassic age (late RP1) of the  
1190 magmatic diking of the rift (Habgood, 1963) upon which the inference of NW-SE-oriented  $\sigma_3$   
1191 was based. We infer that the basement fabrics could have been favorably-oriented for brittle  
1192 exploitation by the early rift border faults within the NW-directed early-RP1 extension  
1193 direction. Such favorably-oriented planes of mechanical weakness in the basement have  
1194 been noted to facilitate the localization of the early-rift border faults in other Karoo rifts that  
1195 were coeval with the SRZ (e.g., Rukwa and Luama Rift; Wheeler and Karson, 1994; Kolawole  
1196 et al., 2021a). This interpretation of basement inheritance is consistent with previous  
1197 observations in different parts of the SRZ (e.g., Cooper and Bloomfield, 1961; Castaing, 1991;  
1198 Williams et al., 2019; Wedmore et al., 2020a) and other rift segments of the East African Rift  
1199 System (Kinabo et al., 2007; Morley, 1999, 2010; Wheeler and Karson, 1989, 1994; Kolawole  
1200 et al., 2018; Heilman et al., 2019).

1201

1202 *5.3.2 Later-Phase (RP3) Border Faulting*

1203 The Cenozoic (RP3) sub-basins in the SRZ: the Lower Shire and Chiuta Sub-basins,  
1204 developed in the hanging walls of border faults with prominent escarpments and along  
1205 which the RP3 sedimentary rift-fill is thickest (Figures 5c-e, 6a-b). However, we note that  
1206 although the southern sections of the Mwanza Fault that are buried beneath Quaternary  
1207 sediments (dashed Mwanza fault trace in Figure 8) do not appear to be active in the current  
1208 rift phase, the northern sections of the fault have been partially reactivated. This partial  
1209 reactivation is inferred from the presence of narrow zones of Quaternary sedimentary cover  
1210 along the northern Mwanza Fault (see Figure 3).

1211 The Thyolo, Muona, Chisumbi, and Camacho faults define distinct segments of a  
1212 system of synthetic border faults along the Lower Shire Graben (Figures 8, 10a-b). All three  
1213 segments show side-stepping geometries among which the Thyolo and Muona segments are  
1214 hard-linked by the Chisumbi segment but soft-linked with the Camacho Fault (Figures 6a-b).  
1215 The northwesternmost segment, the Thyolo Fault, side-steps basinward to the right and  
1216 overlaps with the Muona Fault, which extends ~27 km SE and side-steps to the left towards  
1217 the hinterland where it overlaps with the Camacho Fault (Figure 8). The Camacho Fault  
1218 terminates to the SE near the NE-trending Precambrian Lurio Shear Zone (LSZ) where the  
1219 basin geometry rotates from the NW-SE trend into a N-S trending graben and transitions into  
1220 Urema Graben (Figure 5). These faults are active in the current regional normal faulting  
1221 stress field (Williams et al., 2019). The large-scale alignment of the Thyolo and Muona faults  
1222 with the basement metamorphic fabrics suggests that these border fault segments likely  
1223 localized by exploiting of the basement fabrics at depth (Hodge et al., 2018). It has been  
1224 proposed that the Thyolo border fault likely exploited a Precambrian terrane boundary that  
1225 terminates the Unango Complex to the south (Wedmore et al. (2020a). This interpretation of  
1226 structural inheritance is further supported by the non-optimal orientation of the NW-  
1227 trending basement fabrics to the current ENE-trending regional extension direction  
1228 (Williams et al., 2019).

1229 However, we also find evidence of possible control of rift-orthogonal intra-basement  
1230 structures on the hard- and soft-linkage, and termination of the side-stepping Lower Shire

1231 border fault segments. In the hanging wall of the Thyolo Fault, the aeromagnetic grids reveal  
1232 a magnetic gradient defining a northwestward continuation of the Muona Fault beneath the  
1233 Quaternary sediments (Figures 10a-b). This buried Muona Fault continuation is truncated  
1234 and separated from the exposed southeastern section of the fault by the NE-trending  
1235 Chisumbi Fault which physically connects the exposed Muona Fault to the Thyolo Fault  
1236 (Figures 10a-b). Similarly, the Chisumbi Fault defines the boundary between the  
1237 northwestern section of the Thyolo Fault hanging wall with Quaternary cover from the  
1238 southeastern section where there is no sedimentary cover (Figure 2). Essentially, the  
1239 Chisumbi Fault breached the relay zone between the Thyolo and Muona Faults sometime  
1240 after the faults had been established, and hard-linked them together (also see Wedmore et  
1241 al., 2020a). However, our field data on the strike and dip of the cooled RP1 mafic igneous  
1242 dikes along the rift shoulder (Figure 9civ) shows an alignment of the Chisumbi Fault with the  
1243 intra-basement dikes, suggesting that the hard-linkage of the border fault segments was  
1244 facilitated by the brittle exploitation of the cooled intra-basement dikes (Figure 10b). The  
1245 mechanical contrast created by the mafic dike contacts could have localized the hard-linking  
1246 fault segment. This interpretation is also consistent with a recent field study of the Thyolo-  
1247 Chisumbi-Muona Fault (Wedmore et al., 2020a).

1248 Additional observation of possible brittle deformation localized by the cooled early-  
1249 phase dikes is shown in the filtered aeromagnetic images along the northern and southern  
1250 boundaries of the buried ~60 km-long southern section of the Mwanza Fault. The images  
1251 reveal transverse truncation and offset of the NW-trending fault along the contacts of the  
1252 NE-trending dike lineaments (“T” in Figures S4c and S5b). These truncations are more  
1253 pronounced at the northern tip of the Namalambo Fault where the dikes appear to align with  
1254 and follow the NE-trending basement fabrics along trend (Figure S5b). We interpret that the  
1255 truncating structures are shallow transverse faults that exploited mechanical anisotropies  
1256 within the cooled dike swarms (e.g., dike contacts), consistent with observations elsewhere  
1257 in the North Sea Rift (Phillips et al., 2017). These transverse faults appear as oblique-normal  
1258 faults that cut the pre-existing well-developed border faults in RP3 (Figure S5b), or served  
1259 as side-stepping faults (Figure S4c), to accommodate the subsidence of the Lower Shire  
1260 Graben along the hanging walls of the RP3 border faults as strain has now migrated away

1261 from the older Mwanza-Namalambo border fault. Thus, we suggest that the RP3 subsidence  
1262 and burial of the southern Mwanza Fault, a major long-lived RP1-RP2 border fault of the SRZ  
1263 is related to both the subsidence of the Thyolo-Muona Fault and Panga Fault hanging walls  
1264 and subsidiary faulting along the transverse faults. However, we do not rule out a possibility  
1265 of reactivation of the buried Mwanza Fault segment prior to and after its burial.

1266 At the distal northwest, major border faulting along the SRZ is defined by the Chiuta  
1267 Fault (Figures 5a and 6b) where the fault and its sub-basin developed within a zone of NW-  
1268 trending basement fabrics (Figures 4b and 5a). The alignment of the Chiuta Fault with the  
1269 bounding basement fabrics (Figures 4b, 9a, and 9f) suggests that the nucleation of the fault  
1270 also exploited the basement fabrics.

1271

## 1272 **5.4 Inheritance of Resisting Structures: Transient Barriers to Continuous Lateral** 1273 **Rift Propagation in the Crust**

### 1274 *5.4.1 Rift-Orthogonal Intra-Basement Shear Zones*

1275 Based on basement field studies in the northwestern parts of the SRZ (Barr and  
1276 Brown, 1987; Evans et al., 1999), we suggest that the large-scale bifurcation structure of the  
1277 SRZ and geometry of its branches are influenced by the crustal-scale ENE-trending  
1278 Precambrian Sanangonè Shear Zone (SSZ; Figures 1a-b, and 5a-b). Filtered aeromagnetic grids  
1279 show that the southwestern branch of the SRZ (i.e., the Moatize Sub-basin) terminates at a  
1280 zone of ENE-trending metamorphic fabrics corresponding to gneisses, schists, and diabase  
1281 dikes of the underlying Proterozoic basement terrane (fabrics in the northern parts of Txizita  
1282 Horst in Figures 4b and 9a). Within this zone of termination, the northeastern branch rotates  
1283 counter-clockwise to the west and the Mwanza border fault splays into two NW-trending  
1284 segments near its intersection with the SSZ (Figure 5a). Within this region of border fault  
1285 splay, the basement is exposed, defining a termination of the RP1-RP2 graben along the  
1286 northeastern branch, and we here-in refer to as the 'Machenga Transfer Zone, MTZ' (see  
1287 location in Figures 5a-b). Although the Chiuta Sub-basin is localized to the north of the MTZ,  
1288 its southern bounding fault is oriented ENE-WSW, following the trend of the SSZ (Figure 5b).

1289 Thus, we infer that the initial termination and stagnation of the RP1-RP2 SRZ rift tip  
1290 was controlled by the SSZ which possibly represented a mechanical barrier to continued

1291 early-phase lateral propagation of the rift zone. Also, we note that although in RP3 tectonic  
1292 strain migrated further northwest of the SSZ, represented by the Chiuta Sub-basin, the RP3  
1293 sub-basin also terminates near another zone of ENE-trending basement fabrics with a  
1294 plunging ductile shear zone (Techigoma Shear Zone, TSZ; Figures 4b, 5a, and 5a inset).  
1295 Furthermore, we suggest that the establishment of the Chiuta Sub-basin was facilitated by  
1296 strain localization within an isolated crustal block of NW-trending basement fabrics that is  
1297 located ahead, but proximal to and colinear with the earlier established RP1-RP2 rift zone.  
1298 To the southwest, the RP1-RP2 border fault system either terminates at the NE-trending  
1299 Lurio Shear Zone (Namalambo Fault) or rotates and forms a kink geometry at its intersection  
1300 with the shear zone (Tete Fault System) (see 'NF' and 'TFS' geometries in Figure 5a). We also  
1301 note that the southern tip of the Namalambo Fault rotates clockwise into the NE trend of the  
1302 shear zone. These exhumed intra-basement shear zones are crustal-scale boundaries  
1303 between different basement terranes (Barr and Brown, 1987; Kröner et al., 1997; Evans et  
1304 al., 1999; Bingen et al., 2009). These observations lead us to infer that the rift-orthogonal  
1305 crustal-scale intra-basement shear zones acted as mechanical barriers that influenced the  
1306 initial termination of the Shire Rift Zone during RP1 and RP2, and again terminated the newly  
1307 localized RP3 sub-basin at the northwestern rift tip during the current phase of extension  
1308 (Figures 11a-c). In essence, these shear zones influenced the pulse pattern of multiphase  
1309 lengthening of the rift zone.

1310         The NE trend of the shear zones is misoriented for brittle reactivation in the current  
1311 regional ENE-extension direction, and this 'misorientation' of the mechanical anisotropy  
1312 created by the shear zones may have damped the stress concentration at the propagating rift  
1313 tips. However, we suggest that the lateral variation of crustal strength across the shear zones,  
1314 and the broader rheological domain around the shear zones (e.g., up to 8 km wide zone of  
1315 metamorphic deformation and gabbroic intrusions along the SSZ) most likely influenced the  
1316 temporary stagnation of rift tips near the shear zones. This interpretation is consistent with  
1317 models in Courtillot (1982) which demonstrated that propagating rift tips can become  
1318 stagnated at strong ribbons of the crust referred to as 'locked zones'. Van Wijk and Blackman  
1319 (2004) further showed that the lateral propagation of a rift tip is stalled within strong pre-

1320 rift continental crust, such that during the stall phase, shear stresses progressively build up  
1321 near the rift tip to facilitate a later resumption of lateral rift propagation.

1322         In the SRZ, the counterclockwise rotation and splaying of the Mwanza border fault  
1323 across the SSZ can be interpreted to represent refraction of the propagating border fault  
1324 during the resumption of rift propagation in RP3. This interpretation is consistent with  
1325 observations of normal fault splaying across misoriented crustal terrane boundaries along  
1326 the path of lateral propagation of rift zones in the Great South Basin, New Zealand (Phillips  
1327 et al., 2019b). Numerical models also demonstrate the temporary stagnation of propagating  
1328 rift tips at terrane boundaries that are rift-orthogonal and bound terranes of contrasting  
1329 crustal strength (Phillips et al., 2021). In addition, observations in other areas of early-stage  
1330 continental rifting show that rift zones and their bounding faults terminate at major rift-  
1331 oblique/orthogonal basement shear zones, for example, the termination of the Okavango Rift  
1332 at the Sekaka Shear Zone (Kinabo et al., 2007), and the termination of the Rhino Rift at the  
1333 Aswa Shear Zone (Figure 1a; Katumwehe et al., 2015; Kolawole et al., 2021b). Another  
1334 possible example is the termination of the southern Main Ethiopian Rift at a rift-oblique  
1335 basement terrane (Kounoudis et al., 2021).

1336

#### 1337 *5.4.2 Cooled Early-Rift Mafic dikes*

1338         In addition to the larger scale influence of intra-basement shear zones on rift  
1339 termination, we also note that the cooled early-phase (RP1) magmatic plumbing structures  
1340 of the basement beneath the SRZ may have influenced the arrangement and termination of  
1341 the later phase (RP3) border fault segments. The cooled early-phase dikes did not only  
1342 facilitate the hard-linkage, it appears that the dikes also facilitated the soft-linkage of the  
1343 border fault segments in the Lower Shire Graben (Figures 10a-b). Both the Thyolo and  
1344 Muona Fault segments terminate to the southeast at a zone of conjugate-pattern dike  
1345 clusters consisting of N and NW-trending dike sets (see dike clusters in Figures 10a-b).  
1346 Likewise, the western tip of the Camacho Fault terminates at the Mulata Dike Cluster. We  
1347 interpret that the inherited early phase dikes posed mechanical barriers to the lateral  
1348 propagation of each RP3 border fault segment, resulting in the nucleation of multiple  
1349 synthetic border fault segments that are soft-linked across the zone of conjugate dike cluster.

1350 This may also imply that at this initial stage of development, the maximum lengths of the  
1351 fault segments are delimited by the inherited cooled dikes.

1352 In summary, during the pulsed or episodic propagation of a rift segment, inherited  
1353 intra-basement strength anisotropies can act as both strain-localizing and strain-inhibiting  
1354 tectonic elements within the lithosphere. We suggest that these mechanisms play important  
1355 roles in the evolution of continental rift segment architecture during the early stages of  
1356 continental extension.

1357

## 1358 **6 CONCLUSIONS**

1359 We investigated the large-scale architecture and evolution of the Shire Rift Zone  
1360 (SRZ) over the three phases of tectonic extension (RP1, RP2, and RP3) that are recorded in  
1361 the basin. We compiled and integrated all available surface and subsurface datasets to better  
1362 understand the pre-rift basement structure, major syn-rift depo-centers (sub-basins), the  
1363 border fault structure, and their spatiotemporal distribution. Our results show that although  
1364 the SRZ is characterized by seven major sub-basins, the RP3 (Cenozoic) sub-basins were  
1365 activated at later phase of rifting. Overall, among the seven sub-basins, five are magmatic  
1366 (deposition of volcanics and/or igneous intrusion in sedimentary units) and two are non-  
1367 magmatic. Thus, we infer that the two non-magmatic sub-basins were likely established in  
1368 RP3, the current phase of rifting, during which the RP1-RP2 sub-basins were largely  
1369 abandoned, and strain migrated and localized both at the eastern rift margin and ahead of  
1370 the initial rift termination zone.

1371 We propose that the SRZ propagated in a pulsed manner over the three phases of  
1372 extension, and we provide evidence suggesting that although the border faults largely  
1373 exploited the NW-trending basement metamorphic terrane fabrics, the transient stagnation  
1374 zones of the rift tips during each rift phase were influenced by rift-orthogonal terrane  
1375 boundary shear zones. In essence, we argue that during the pulsed propagation of a  
1376 continental rift segment, inherited strength anisotropies can serve as both strain-localizing,  
1377 refracting, and possibly, temporarily strain-inhibiting tectonic elements in the lithosphere.

1378

1379

1380 **ACKNOWLEDGEMENTS**

1381 We thank Jack Williams and Ake Fagereng for their comments on the earlier versions of this  
1382 manuscript which helped to improve the quality of the paper. Thanks to the Geological  
1383 Survey of Malawi for providing the 2013 aeromagnetic datasets used in this study. Thanks  
1384 also to the Council for Geoscience, South Africa, for providing the South African Development  
1385 Community (SADC) regional aeromagnetic dataset used in this study. We thank Elias  
1386 Chikalamo, Patrick R. N. Chindandali, Lois Kamuyango, Wesley T. Prater, Amy R. Pritt,  
1387 Alejandra Santiago-Torres, and Kevin Vélez-Rosado for collecting field structural data in  
1388 southern Malawi. We also thank Jalf Salima and Leonard Kalindekafe for supporting the  
1389 logistics of our fieldwork. This research was supported by the NSF Grant No. II-1358150 and  
1390 EAR 1255233.

1391

1392 **DATA AVAILABILITY**

1393 The Shuttle Radar Topography Mission (SRTM) dataset used in this study can be freely  
1394 obtained from the United States Geological Survey database <https://earthexplorer.usgs.gov>.  
1395 The southern Malawi Total Magnetic Intensity (TMI) dataset can be freely obtained from the  
1396 Interdisciplinary Earth Data Alliance (IEDA) at doi:10.1594/IEDA/324860 (Nyalugwe et al.,  
1397 2019b).

1398 **REFERENCES**

- 1399 Addison, M.J., Rivett, M.O., Phiri, O.L., Milne, N., Milne, V., McMahon, A.D., Macpherson, L.,  
1400 Bagg, J., Conway, D.I., Phiri, P. and Mbalame, E., 2021. 'Hidden Hot Springs' as a Source of  
1401 Groundwater Fluoride and Severe Dental Fluorosis in Malawi. *Water*, 13(8), p.1106.
- 1402 Arkani-Hamed, J. (1988). Differential reduction-to-the-pole of regional magnetic anomalies.  
1403 *Geophysics*, 53(12), 1592–1600.
- 1404 Barr, M.W.C. and Brown, M.A., 1987. Precambrian gabbro–anorthosite complexes, Tete  
1405 Province, Mozambique. *Geological Journal*, 22(S2), pp.139-159.
- 1406 Bell, R.E., Jackson, C.A.L., Whipp, P.S. and Clements, B., 2014. Strain migration during  
1407 multiphase extension: Observations from the northern North Sea. *Tectonics*, 33(10),  
1408 pp.1936-1963.
- 1409 Baranov, V. (1957). A new method for interpretation of aeromagnetic maps: Pseudo-  
1410 gravimetric anomalies. *Geophysics*, 22(2), 359–382.
- 1411 Bennett, J. D. (1989). Smaller Coal Basins in Africa Project - Final Report: Review of Lower  
1412 Karoo coal basins and coal resource development in parts of central and southern Africa with  
1413 particular reference to northern Malawi. British Geological Survey Technical Report  
1414 WC/89/21.
- 1415 Bergh, S.G., Eig, K., Kløvjan, O.S., Henningsen, T., Olesen, O. and Hansen, J.A., 2007. The  
1416 Lofoten-Vesterålen continental margin: a multiphase Mesozoic-Palaeogene rifted shelf as  
1417 shown by offshore-onshore brittle fault-fracture analysis. *Norwegian Journal of*  
1418 *Geology/Norsk Geologisk Forening*, 87.
- 1419 Bingen, B., Jacobs, J., Viola, G., Henderson, I.H.C., Skår, Ø., Boyd, R., Thomas, R.J., Solli, A., Key,  
1420 R.M. and Daudi, E.X.F., 2009. Geochronology of the Precambrian crust in the Mozambique  
1421 belt in NE Mozambique, and implications for Gondwana assembly. *Precambrian Research*,  
1422 170(3-4), pp.231-255.
- 1423 Bjorlykke, K., 1989. *Sedimentology and petroleum geology*. Springer Berlin Heidelberg.  
1424 363p.
- 1425 Bloomfield, K., 1958. *The geology of the Port Herald area*. Malawi Geological Survey  
1426 Department Bulletin 9, Zomba.
- 1427 Braun, J. (1992). Post-extensional mantle healing and episodic extension in the Canning  
1428 Basin. *Journal of Geophysical Research*, 97(B6), 8927.
- 1429 Brune, S., Heine, C., Pérez-Gussinyé, M. and Sobolev, S.V., 2014. Rift migration explains  
1430 continental margin asymmetry and crustal hyper-extension. *Nature communications*, 5(1),  
1431 pp.1-9.
- 1432 Burke, K., Ashwal, L.D. and Webb, S.J., 2003. New way to map old sutures using deformed  
1433 alkaline rocks and carbonatites. *Geology*, 31(5), pp.391-394.
- 1434 Castaing, C. (1991), Post-Pan-African tectonic evolution of South Malawi in relation to the  
1435 Karroo and recent East African rift systems. *Tectonophysics*, 191(1-2), pp.55-73.

- 1436 Chisenga, C., Dulanya, Z. and Jianguo, Y. (2019), The structural re-interpretation of the Lower  
1437 Shire Basin in the Southern Malawi rift using gravity data. *Journal of African Earth Sciences*,  
1438 149, pp.280-290.
- 1439 Chorowicz, J., 2005. The east African rift system. *Journal of African Earth Sciences*, 43(1-3),  
1440 pp.379-410.
- 1441 Choubert, G., Faure-Muret, A., Chanteux, P., Roche, G., Simpson, E.S.W., Shackleton, L.,  
1442 Ségoufin, J., Seguin, C. and Sougy, J., 1988. International geological map of Africa. Scale 1:  
1443 5,000,000, Commission for the Geological Map of the World (CGMW), Unesco, Paris.
- 1444 Cooper, W.G.G., and Bloomfield, K. 1961. The geology of the Tambani-Salambidwe area.  
1445 Malawi Geological Survey Department Bulletin 13, Zomba.
- 1446 Corti, G., 2004. Centrifuge modelling of the influence of crustal fabrics on the development of  
1447 transfer zones: insights into the mechanics of continental rifting architecture.  
1448 *Tectonophysics*, 384(1-4), pp.191-208.
- 1449 Corti, G., 2012. Evolution and characteristics of continental rifting: Analog modeling-inspired  
1450 view and comparison with examples from the East African Rift System. *Tectonophysics*, 522,  
1451 pp.1-33.
- 1452 Corti, G., van Wijk, J., Cloetingh, S. and Morley, C.K., 2007. Tectonic inheritance and  
1453 continental rift architecture: Numerical and analogue models of the East African Rift system.  
1454 *Tectonics*, 26(6).
- 1455 Courtillot, V. (1982). Propagating rifts and continental breakup. *Tectonics*, 1(3), 239–250.  
1456 <https://doi.org/10.1029/TC001i003p00239>
- 1457 Daly, M.C., Chorowicz, J. and Fairhead, J.D., 1989. Rift basin evolution in Africa: the influence  
1458 of reactivated steep basement shear zones. Geological Society, London, Special Publications,  
1459 44(1), pp.309-334.
- 1460 Daly, M. C., Green, P., Watts, A. B., Davies, O., Chibesakunda, F., & Walker, R. (2020). Tectonics  
1461 and Landscape of the Central African Plateau, and their implications for a propagating  
1462 Southwestern Rift in Africa. *Geochemistry, Geophysics, Geosystems*, 21, e2019GC008746.  
1463 <https://doi.org/10.1029/2019G C008746>
- 1464 Daly, M.C., Lawrence, S.R., Kimun'a, D. and Binga, M., 1991. Late Palaeozoic deformation in  
1465 central Africa: a result of distant collision?. *Nature*, 350(6319), pp.605-607.
- 1466 Daszinnies, M.C., Emmel, B., Jacobs, J., Grantham, G.H. and Thomas, R.J., 2008. Denudation in  
1467 southern Malawi and northern Mozambique: indications of the long-term tectonic  
1468 segmentation of East Africa during Gondwana break-up.
- 1469 Delvaux, D., 1989. The Karoo to Recent rifting in the western branch of the East-African Rift  
1470 System: A bibliographical synthesis. *Mus. roy. Afr. centr., Tervuren (Belg.), Dépt. Géol. Min.,*  
1471 *Rapp. ann, 1990 (1991)*, pp.63-83.
- 1472 Delvaux, D., 2001. Karoo rifting in western Tanzania: precursor of Gondwana break-up.  
1473 *Contributions to geology and paleontology of Gondwana in honor of Helmut Wopfner:*  
1474 *Cologne, Geological Institute, University of Cologne*, pp.111-125.

- 1475 Dixey F. 1925. The Physiography of the Shire Valley, Nyasaland. Rep. Geol. Surv. Dept.,  
1476 Nyasaland Proto.
- 1477 Donath, F.A., 1961. Experimental study of shear failure in anisotropic rocks. Geological  
1478 Society of America Bulletin, 72(6), pp.985-989.
- 1479 Duffy, O.B., Bell, R.E., Jackson, C.A.L., Gawthorpe, R.L. and Whipp, P.S., 2015. Fault growth and  
1480 interactions in a multiphase rift fault network: Horda Platform, Norwegian North Sea.  
1481 Journal of Structural Geology, 80, pp.99-119.
- 1482 Dulanya, Z., 2017. A review of the geomorphotectonic evolution of the south Malawi rift.  
1483 Journal of African Earth Sciences, 129, pp.728-738.
- 1484 Ebinger, C.J., Yemane, T., Harding, D.J., Tesfaye, S., Kelley, S. and Rex, D.C., 2000. Rift  
1485 deflection, migration, and propagation: Linkage of the Ethiopian and Eastern rifts, Africa.  
1486 Geological Society of America Bulletin, 112(2), pp.163-176.
- 1487 Evans, R.J., Ashwal, L.D. and Hamilton, M.A., 1999. Mafic, ultramafic, and anorthositic rocks  
1488 of the Tete Complex, Mozambique: petrology, age, and significance. South African Journal of  
1489 Geology, 102(2), pp.153-166.
- 1490 Fazlikhani, H., Aagotnes, S.S., Refvem, M.A., Hamilton-Wright, J., Bell, R., Fossen, H.,  
1491 Gawthorpe, R.L., Jackson, C.A.L. and Rotevatn, A., 2020. Strain migration during multiphase  
1492 extension, Stord Basin, northern North Sea rift. arXiv, 6 June 2020, Web:  
1493 <https://eartharxiv.org/b8acf/>
- 1494 Fontijn, K., Delvaux, D., Ernst, G. G., Kervyn, M., Mbede, E., & Jacobs, P. (2010). Tectonic control  
1495 over active volcanism at a range of scales: Case of the Rungwe Volcanic Province, SW  
1496 Tanzania; and hazard implications. Journal of African Earth Sciences, 58(5), 764–777.
- 1497 Ford, M., Hemelsdaël, R., Mancini, M. and Palyvos, N., 2017. Rift migration and lateral  
1498 propagation: evolution of normal faults and sediment-routing systems of the western  
1499 Corinth rift (Greece). Geological Society, London, Special Publications, 439(1), pp.131-168.
- 1500 Fritz, H., Abdelsalam, M., Ali, K. A., Bingen, B., Collins, A. S., Fowler, A. R., et al. (2013). Orogen  
1501 styles in the East African Orogen: A review of the Neoproterozoic to Cambrian tectonic  
1502 evolution. Journal of African Earth Sciences, 86, 65–106.
- 1503 Gawthorpe, R., Leeder, M., 2000. Tectono-sedimentary evolution of active extensional basins.  
1504 Basin Res. 12, 195e218.
- 1505 Habgood, F. (1963). The geology of the country west of the Shire River between Chikwawa  
1506 and Chiromo. Malawi Geological Survey Department Bulletin No. 14, Zomba.
- 1507 Habgood, F., Holt, D. N., and Walshaw, R.D., 1973. The Geology of the Thyolo Area. Malawi  
1508 Geological Survey Department Bulletin No. 22, Zomba.
- 1509 Hargrove, U.S., Hanson, R.E., Martin, M.W., Blenkinsop, T.G., Bowring, S.A., Walker, N. and  
1510 Munyanyiwa, H., 2003. Tectonic evolution of the Zambezi orogenic belt: geochronological,  
1511 structural, and petrological constraints from northern Zimbabwe. Precambrian Research,  
1512 123(2-4), pp.159-186.

- 1513 Heilman, E., Kolawole, F., Atekwana, E.A. and Mayle, M., 2019. Controls of Basement fabric on  
1514 the Linkage of Rift Segments. *Tectonics*, 38(4), pp.1337-1366.
- 1515 Henstra, G.A., Rotevatn, A., Gawthorpe, R.L. and Ravnås, R., 2015. Evolution of a major  
1516 segmented normal fault during multiphase rifting: the origin of plan-view zigzag geometry.  
1517 *Journal of Structural Geology*, 74, pp.45-63.
- 1518 Heron, P.J., Peace, A.L., McCaffrey, K.J.W., Welford, J.K., Wilson, R., van Hunen, J. and  
1519 Pysklywec, R.N., 2019. Segmentation of rifts through structural inheritance: Creation of the  
1520 Davis Strait. *Tectonics*, 38(7), pp.2411-2430.
- 1521 Hodge, M., Fagereng, Å., Biggs, J., & Mdala, H. (2018). Controls on early-rift geometry: New  
1522 perspectives from the Bilila-Mtakataka Fault, Malawi. *Geo-physical Research Letters*, 45(9),  
1523 3896-3905.
- 1524 Hunt, J.M., Philp, R.P. and Kvenvolden, K.A., 2002. Early developments in petroleum  
1525 geochemistry. *Organic geochemistry*, 33(9), pp.1025-1052.
- 1526 Jones-Cecil, M., 1995. Structural controls of Holocene reactivation of the Meers fault,  
1527 southwestern Oklahoma, from magnetic studies. *Geological Society of America Bulletin*,  
1528 107(1), pp.98-112.
- 1529 Katumwehe, A.B., Abdelsalam, M.G. and Atekwana, E.A., 2015. The role of pre-existing  
1530 Precambrian structures in rift evolution: The Albertine and Rhino grabens, Uganda.  
1531 *Tectonophysics*, 646, pp.117-129.
- 1532 Keep, M. and McClay, K.R., 1997. Analogue modelling of multiphase rift systems.  
1533 *Tectonophysics*, 273(3-4), pp.239-270.
- 1534 Kinabo, B. D., Atekwana, E. A., Hogan, J. P., Modisi, M. P., Wheaton, D. D., & Kampunzu, A. B.  
1535 (2007). Early structural development of the Okavango rift zone, NW Botswana. *Journal of*  
1536 *African Earth Sciences*, 48(2-3), 125–136.
- 1537 Kinabo, B.D., Atekwana, E.A., Hogan, J.P., Modisi, M.P., Wheaton, D.D. and Kampunzu, A.B.,  
1538 2007. Early structural development of the Okavango rift zone, NW Botswana. *Journal of*  
1539 *African Earth Sciences*, 48(2-3), pp.125-136.
- 1540 Kolawole, F., Atekwana, E.A., Laó-Dávila, D.A., Abdelsalam, M.G., Chindandali, P.R., Salima, J.  
1541 and Kalindekafe, L., 2018. Active deformation of Malawi rift's north basin Hinge zone  
1542 modulated by reactivation of preexisting Precambrian Shear zone fabric. *Tectonics*, 37(3),  
1543 pp.683-704.
- 1544 Kolawole, F., Phillips, T.B., Atekwana, E.A. and Jackson, C.A.L., 2021a. Structural inheritance  
1545 controls strain distribution during early continental rifting, rukwa rift. *Frontiers in Earth*  
1546 *Science*, p.670.
- 1547 Kolawole, F., Firkins, M. C., Al Wahaibi, T. S., Atekwana, E. A., & Soreghan, M. J. (2021b). Rift  
1548 interaction zones and the stages of rift linkage in active segmented continental rift systems.  
1549 *Basin Research*, 33, 2984– 3020. <https://doi.org/10.1111/bre.12592>
- 1550 Kounoudis, R., Bastow, I.D., Ebinger, C.J., Ogden, C.S., Ayele, A., Bendick, R., Mariita, N., Kianji,  
1551 G., Wigham, G., Musila, M. and Kibret, B., 2021. Body-Wave Tomographic Imaging of the

- 1552 Turkana Depression: Implications for Rift Development and Plume-Lithosphere  
1553 Interactions. *Geochemistry, Geophysics, Geosystems*, 22(8), p.e2021GC009782.
- 1554 Kröner, A., Sacchi, R., Jaeckel, P., Costa, M., 1997. Kibaran magmatism and Pan-African  
1555 granulite metamorphism in northern Mozambique: single zircon ages and regional  
1556 implications. *Journal of African Earth Sciences* 25, 467–484.
- 1557 Laó-Dávila, D. A., Al-Salmi, H. S., Abdelsalam, M. G., & Atekwana, E. A. (2015). Hierarchical  
1558 segmentation of the Malawi Rift: The influence of inherited lithospheric heterogeneity and  
1559 kinematics in the evolution of continental rifts. *Tectonics*, 34, 2399–2417.
- 1560 Lemna, O.S., Stephenson, R. and Cornwell, D.G., 2019. The role of pre-existing Precambrian  
1561 structures in the development of Rukwa Rift Basin, southwest Tanzania. *Journal of African*  
1562 *Earth Sciences*, 150, pp.607-625.
- 1563 Ma, G. Q., Du, X. J., Li, L. L., & Meng, L. S. (2012). Interpretation of magnetic anomalies by  
1564 horizontal and vertical derivatives of the analytic signal. *Applied Geophysics*, 9(4), 468–474.
- 1565 Mardia, K.V. and Jupp, P.E., 2009. *Directional statistics*. Vol. 494, John Wiley & Sons, West  
1566 Sussex, England.
- 1567 Manatschal, G., Lavier, L. and Chenin, P., 2015. The role of inheritance in structuring  
1568 hyperextended rift systems: Some considerations based on observations and numerical  
1569 modeling. *Gondwana Research*, 27(1), pp.140-164.
- 1570 Modisi, M.P., Atekwana, E.A., Kampunzu, A.B. and Ngwisanyi, T.H., 2000. Rift kinematics  
1571 during the incipient stages of continental extension: Evidence from the nascent Okavango  
1572 rift basin, northwest Botswana. *Geology*, 28(10), pp.939-942.
- 1573 Mohriak, W.U. and Leroy, S., 2013. Architecture of rifted continental margins and break-up  
1574 evolution: insights from the South Atlantic, North Atlantic and Red Sea–Gulf of Aden  
1575 conjugate margins. *Geological Society, London, Special Publications*, 369(1), pp.497-535.
- 1576 Morley, C. K. (1999). Influence of preexisting fabrics on rift structure. In C. K. Morley (Ed.),  
1577 *Geoscience of Rift Systems—Evolution of East Africa*, AAPG Studies in Geology (Vol. 44, pp.  
1578 151–160).
- 1579 Morley, C. K. (2010). Stress re-orientation along zones of weak fabrics in rifts: An explanation  
1580 for pure extension in ‘oblique’ rift segments? *Earth and Planetary Science Letters*, 297(3-4),  
1581 667–673.
- 1582 Naliboff, J., & Buitter, S. J. H. (2015). Rift reactivation and migration during multiphase  
1583 extension. *Earth and Planetary Science Letters*, 421, 58–67.
- 1584 Nelson, R.A., Patton, T.L. and Morley, C.K., 1992. Rift-segment interaction and its relation to  
1585 hydrocarbon exploration in continental rift systems (1). *AAPG bulletin*, 76(8), pp.1153-1169.
- 1586 Njinju, E.A., Atekwana, E.A., Stamps, D.S., Abdelsalam, M.G., Atekwana, E.A., Mickus, K.L.,  
1587 Fishwick, S., Kolawole, F., Rajaonarison, T.A. and Nyalugwe, V.N., 2019a. Lithospheric  
1588 structure of the Malawi Rift: Implications for magma-poor rifting processes. *Tectonics*,  
1589 38(11), pp.3835-3853.
- 1590 Njinju, E.A., Kolawole, F., Atekwana, E.A., Stamps, D.S., Atekwana, E.A., Abdelsalam, M.G. and  
1591 Mickus, K.L., 2019b. Terrestrial heat flow in the Malawi Rifted Zone, East Africa: Implications

- 1592 for tectono-thermal inheritance in continental rift basins. *Journal of Volcanology and*  
1593 *Geothermal Research*, 387, p.106656.
- 1594 Nyalugwe, V.N., Abdelsalam, M.G., Atekwana, E.A., Katumwehe, A., Mickus, K.L., Salima, J.,  
1595 Njinju, E.A. and Emishaw, L. (2019a). Lithospheric structure beneath the Cretaceous Chilwa  
1596 Alkaline Province (CAP) in southern Malawi and northeastern Mozambique. *Journal of*  
1597 *Geophysical Research: Solid Earth*, 124(11), pp.12224-12240.
- 1598 Nyalugwe, V.; Abdelsalam, M.; Atekwana, E.; Katumwehe, A.; Mickus, K.; Salima, J.; Njinju, E.  
1599 and L. Emishaw, (2019b). 2013 Total Magnetic Intensity (TMI) gridded aeromagnetic data  
1600 of southern Malawi 34 45 E – 36 00 E and 14 45 S and 16 15 S (investigator Mohamed  
1601 Abdelsalam). *Interdisciplinary Earth Data Alliance (IEDA)*. doi:10.1594/IEDA/324860.
- 1602 Nyalugwe, V.N., Abdelsalam, M.G., Katumwehe, A., Mickus, K.L. and Atekwana, E.A. (2020).  
1603 Structure and tectonic setting of the Chingale Igneous Ring Complex, Malawi from  
1604 aeromagnetic and satellite gravity data: Implication for Precambrian terranes collision and  
1605 Neogene-Quaternary rifting. *Journal of African Earth Sciences*, 163, p.103760.
- 1606 Oesterlen, P.M. and Blenkinsop, T.G., 1994. Extension directions and strain near the failed  
1607 triple junction of the Zambezi and Luangwa Rift zones, southern Africa. *Journal of African*  
1608 *Earth Sciences*, 18(2), pp.175-180.
- 1609 Ojo, O., Laó-Dávila, D.A. and Thomson, S.N., 2020. Thermotectonic History of the Southern  
1610 Malawi Rift and Northern Shire Graben Border Faults: Insights From Apatite Fission Tracks  
1611 and Remote Sensing Analyses. In *AGU Fall Meeting Abstracts (Vol. 2020, pp. T024-0010)*.
- 1612 Osagiede, E.E., Rotevatn, A., Gawthorpe, R., Kristensen, T.B., Jackson, C.A. and Marsh, N., 2020.  
1613 Pre-existing intra-basement shear zones influence growth and geometry of non-colinear  
1614 normal faults, western Utsira High–Heimdal Terrace, North Sea. *Journal of Structural*  
1615 *Geology*, 130, p.103908.
- 1616 Phillips, T.B., Fazlikhani, H., Gawthorpe, R.L., Fossen, H., Jackson, C.A.L., Bell, R.E., Faleide, J.I.  
1617 and Rotevatn, A., 2019a. The Influence of Structural Inheritance and Multiphase Extension  
1618 on Rift Development, the Northern North Sea. *Tectonics*, 38.
- 1619 Phillips, T.B., Magee, C., Jackson, C.A.L. and Bell, R.E., 2018. Determining the three-  
1620 dimensional geometry of a dike swarm and its impact on later rift geometry using seismic  
1621 reflection data. *Geology*, 46(2), pp.119-122.
- 1622 Phillips, T. B., and McCaffrey, K. J. W. (2019b). Terrane Boundary Reactivation, Barriers to  
1623 Lateral Fault Propagation and Reactivated Fabrics: Rifting across the Median Batholith Zone,  
1624 Great South Basin, New Zealand. *Tectonics* 38 (11), 4027–4053. doi:10.1029/2019tc005772
- 1625 Phillips, T.B., Naliboff, J., McCaffrey, K., Pan, S., and van Hunen, J., 2021. The influence of  
1626 crustal strength on rift geometry and development–Insights from 3D numerical modelling.
- 1627 Ragland, P.C., Hatcher Jr, R.D. and Whittington, D., 1983. Juxtaposed Mesozoic diabase dike  
1628 sets from the Carolinas: A preliminary assessment. *Geology*, 11(7), pp.394-399.
- 1629 Ranalli, G. and Yin, Z.M., 1990. Critical stress difference and orientation of faults in rocks with  
1630 strength anisotropies: the two-dimensional case. *Journal of Structural geology*, 12(8),  
1631 pp.1067-1071.

- 1632 Ring, U., 1995. Tectonic and lithological constraints on the evolution of the Karoo graben of  
1633 northern Malawi (East Africa). *Geologische Rundschau*, 84(3), pp.607-625.
- 1634 Rotevatn, A., Kristensen, T., Ksienzyk, A., Wemmer, K., Henstra, G., Midtkandal, I., Grundvåg,  
1635 S.A., Andresen, A., 2018. Structural inheritance and rapid rift-length establishment in a  
1636 multiphase rift: the East Greenland rift system and its Caledonian orogenic ancestry.  
1637 *Tectonics* 37, 1858–1875.
- 1638 Ryan, W. B. F., S.M. Carbotte, J. Coplan, S. O'Hara, A. Melkonian, R. Arko, R.A. Weissel, V.  
1639 Ferrini, A. Goodwillie, F. Nitsche, J. Bonczkowski, and R. Zemsky (2009), Global Multi-  
1640 Resolution Topography (GMRT) synthesis data set, *Geochem. Geophys. Geosyst.*, 10, Q03014.
- 1641 Sacchi, R., Cadoppi, P. and Costa, M., 2000. Pan-African reactivation of the Lurio segment of  
1642 the Kibaran Belt system: a reappraisal from recent age determinations in northern  
1643 Mozambique. *Journal of African Earth Sciences*, 30(3), pp.629-639.
- 1644 Scholz, C.A., Shillington, D.J., Wright, L.J., Accardo, N., Gaherty, J.B. and Chindandali, P., 2020.  
1645 Intrarift fault fabric, segmentation, and basin evolution of the Lake Malawi (Nyasa) Rift, East  
1646 Africa. *Geosphere*.
- 1647 Singh, A.K., Singh, M.P., Sharma, M. and Srivastava, S.K., 2007. Microstructures and  
1648 microtextures of natural cokes: a case study of heat-affected coking coals from the Jharia  
1649 coalfield, India. *International Journal of Coal Geology*, 71(2-3), pp.153-175.
- 1650 Smets, B., Delvaux, D., Ross, K.A., Poppe, S., Kervyn, M., d'Oreye, N. and Kervyn, F. (2016). The  
1651 role of inherited crustal structures and magmatism in the development of rift segments:  
1652 Insights from the Kivu basin, western branch of the East African Rift. *Tectonophysics*, 683,  
1653 pp.62-76.
- 1654 Stamps, D.S., Saria, E. and Kreemer, C. (2018). A geodetic strain rate model for the East  
1655 African Rift system. *Scientific reports*, 8(1), pp.1-8.
- 1656 Stevens, V.L., Sloan, R.A., Chindandali, P.R., Wedmore, L.N., Salomon, G.W. and Muir, R.A.,  
1657 2021. The Entire Crust can be Seismogenic: Evidence from Southern Malawi. *Tectonics*,  
1658 p.e2020TC006654.
- 1659 Stewart, A.K., Massey, M., Padgett, P.L., Rimmer, S.M. and Hower, J.C., 2005. Influence of a  
1660 basic intrusion on the vitrinite reflectance and chemistry of the Springfield (No. 5) coal,  
1661 Harrisburg, Illinois. *International Journal of Coal Geology*, 63(1-2), pp.58-67.
- 1662 Suárez-Ruiz, I. and Crelling, J.C. eds., 2008. *Applied coal petrology: the role of petrology in*  
1663 *coal utilization*. 1st edition, Academic press, Elsevier Ltd, New York. 408p.  
1664 <https://doi.org/10.1016/B978-0-08-045051-3.X0001-2>
- 1665 Trouw, R.A. and De Wit, M.J., 1999. Relation between the Gondwanide Orogen and  
1666 contemporaneous intracratonic deformation. *Journal of African Earth Sciences*, 28(1),  
1667 pp.203-213.
- 1668 Versfelt, J.W. (2009), South Atlantic margin rift basin asymmetry and implications for pre-  
1669 salt exploration. International Petroleum Technology Conference (IPTC) paper 13833, Doha,  
1670 Qatar.

- 1671 Wheeler, W. H., & Karson, J. A. (1989). Structure and kinematics of the Livingstone Mountains  
1672 border fault zone, Nyasa (Malawi) Rift, southwestern Tanzania. *Journal of African Earth*  
1673 *Sciences (and the Middle East)*, 8(2–4), 393–413.
- 1674 Wheeler, W.H. and Karson, J.A., 1994. Extension and subsidence adjacent to a "weak"  
1675 continental transform: An example from the Rukwa rift, East Africa. *Geology*, 22(7), pp.625-  
1676 628.
- 1677 Williams, J.N., Fagereng, Å., Wedmore, L.N., Biggs, J., Mphepo, F., Dulanya, Z., Mdala, H. and  
1678 Blenkinsop, T., 2019. How do variably striking faults reactivate during rifting? Insights from  
1679 southern Malawi. *Geochemistry, Geophysics, Geosystems*, 20(7), pp.3588-3607.
- 1680 Williams, J.N., Mdala, H., Fagereng, Å., Wedmore, L.N., Biggs, J., Dulanya, Z., Chindandali, P.  
1681 and Mphepo, F., 2021. A systems-based approach to parameterise seismic hazard in regions  
1682 with little historical or instrumental seismicity: active fault and seismogenic source  
1683 databases for southern Malawi. *Solid Earth*, 12(1), pp.187-217.
- 1684 Wedmore, L.N., Williams, J.N., Biggs, J., Fagereng, Å., Mphepo, F., Dulanya, Z., Willoughby, J.,  
1685 Mdala, H. and Adams, B., 2020a. Structural inheritance and border fault reactivation during  
1686 active early-stage rifting along the Thyolo fault, Malawi. *Journal of Structural Geology*,  
1687 p.104097.
- 1688 Wedmore, L.N., Biggs, J., Williams, J.N., Fagereng, Å., Dulanya, Z., Mphepo, F. and Mdala, H.,  
1689 2020b. Active fault scarps in southern Malawi and their implications for the distribution of  
1690 strain in incipient continental rifts. *Tectonics*, 39(3), p.e2019TC005834.
- 1691 Wedmore, L.N., Biggs, J., Floyd, M., Fagereng, Å., Mdala, H., Chindandali, P., Williams, J.N. and  
1692 Mphepo, F., 2021. Geodetic constraints on cratonic microplates and broad strain during  
1693 rifting of thick Southern African lithosphere. *Geophysical Research Letters*, 48(17),  
1694 p.e2021GL093785.
- 1695 Westerhof, A.P., Lehtonen, M.I., Mäkitie, H., Manninen, T., Pekkala, Y., Gustafsson, B. and  
1696 Tahon, A., 2008. The Tete-Chipata Belt: A new multiple terrane element from western  
1697 Mozambique and southern Zambia. *Geological Survey of Finland Special Paper*, 48, pp.145-  
1698 166.
- 1699 Woolley, A. R., Bevan, J. C. and Elliott, C. J. (1979). The Karroo dolerites of southern Malawi  
1700 and their regional geochemical implications. *Mineralogical Magazine*, 43(328), p.487-495.
- 1701 Youash, Y., 1969. Tension tests on layered rocks. *Geological Society of America Bulletin*,  
1702 80(2), pp.303-306.